JOURNAL OF PETROLOGY

Journal of Petrology, 2015, Vol. 56, No. 1, 59–81
doi: 10.1093/petrology/egu071
Original Article

OXFORD

The Role of Late Sulfide Saturation in the Formation of a Cu- and Au-rich Magma: Insights from the Platinum Group Element Geochemistry of Niuatahi–Motutahi Lavas, Tonga Rear Arc

Jung-Woo Park[1]*, Ian H. Campbell[1], Jonguk Kim[2] and Jai-Woon Moon[2]

[1]Research School of Earth Sciences, Australian National University, Canberra, ACT 2601, Australia and [2]Deep-Sea and Seabed Resources Research Division, Korea Institute of Ocean Science & Technology, 787 Haeanro, Ansan, 426-744, South Korea

*Corresponding author. E-mail: jung.park@anu.edu.au

Received May 5, 2014; Accepted November 25, 2014

ABSTRACT

Magmas enriched in Cu and Au are likely to be the most prospective for magmatic–hydrothermal deposits of these metals. However, the mechanism that leads to the formation of metal-rich magmas is not well constrained. We report major, trace and platinum group element (PGE) data for the Niuatahi–Motutahi lavas, Tonga rear arc, with the aim of studying their petrogenesis with special emphasis on the evolution of chalcophile elements during magmatic differentiation. Major and trace element contents, including S and Cl, were also measured in glasses, phenocrysts and melt inclusions to complement the whole-rock data. The Niuatahi–Motutahi lavas are associated with Cu and Au mineralization and therefore provide an opportunity to investigate the characteristics of an ore-associated magmatic system. They show a wide compositional variation from basalts to dacites with MgO contents that vary between ~14 and 1 wt %. The dacites can be subdivided into high-K and low-K dacites. Geochemical modeling and their mineralogy suggest that the low-K dacites are comagmatic with the basalts and evolved by fractional crystallization. Copper, Au and Pd behave incompatibly in the basalts and andesitic glasses, whereas they become compatible in the low-K dacite. In contrast, Pt, Rh, Ru and Ir are moderately compatible in the basalts and correlate negatively with MgO, but become strongly compatible in the dacites. The Cu, Au and PGE trends can be explained by fractional crystallization of a Pt-rich alloy in the basalts and andesitic glasses, followed by sulfide saturation in the low-K dacites. The high-K dacites may have evolved from a slightly different magma source; however, their chalcophile elements fractionated in a similar manner. Chlorine and S data for melt inclusions and glasses from the basalts and dacites suggest that water-rich volatile saturation occurred during evolution of the dacites. The Niuatahi–Motutahi dacites were enriched in Cu from 80 to 200 ppm and in Au from <1 to 7 ppb by fractional crystallization as the magma evolved from basalt through andesite to dacite. We suggest that late sulfide saturation allowed Cu and Au to become enriched by a factor of two in the Niuatahi–Motutahi dacites before volatile saturation and that this played an important role in the formation of the Cu- and Au-rich mineralization. This sulfide saturation history contrasts with that of the Honshu arc volcanic rocks, Japan, where sulfide saturation occurred early. The Honshu arc volcanic rocks are not associated with porphyry Cu or Au deposits, which we suggest is due to loss of most of the Cu and Au to an early immiscible sulfide phase.

Downloaded from http://petrology.oxfordjournals.org/ by guest on January 20, 2015

© The Author 2015. Published by Oxford University Press. All rights reserved. For Permissions, please e-mail: journals.permissions@oup.com

Key words: Cu-rich magma genesis; Au-rich magma genesis; magmatic–hydrothermal deposit; platinum group element; sulfide saturation; volatile exsolution

INTRODUCTION

Magmatic–hydrothermal ore deposits such as porphyry, skarn and high-sulfidation epithermal deposits are spatially and temporally related to intermediate to felsic arc magmas, which are considered to be the dominant source of ore metals (Robb, 2005). However, most arc magmas are not associated with economic ore deposits. The obvious question is: 'Why are some arc magmatic systems ore-bearing whereas others are barren?' Is it because some arc-related magmas are initially enriched in the ore metals such as Cu and Au and therefore more likely to form a deposit (e.g. Mungall, 2002; Sun *et al.*, 2011), or is the magma differentiation process more critical than the initial ore metal concentration (e.g. Richards, 2003; Jenner *et al.*, 2010; Park *et al.*, 2013*a*)?

The ore metals in a magmatic–hydrothermal ore deposit are carried to the site of deposition by a volatile phase exsolved from a magma chamber (Hedenquist & Lowenstern, 1994; Candela, 1997; Williams-Jones & Heinrich, 2005; Mavrogenes *et al.*, 2010). During this process, competition for ore metals between the volatile phase and crystallizing minerals during magma evolution is a primary factor in the formation of a metal-rich volatile phase, assuming that the magmatic vapor has an appropriate composition and that precipitation of the metals occurs in a confined area (Candela, 1997). In sulfide-saturated magmas an immiscible sulfide melt is the critical phase competing for Cu and Au with the exsolving volatile phase owing to the high partition coefficients of these elements between sulfide and silicate melts. If a magma experienced prolonged sulfide melt segregation before volatile saturation, the magma is unlikely to form a magmatic–hydrothermal Cu–Au deposit, as most of the budget of chalcophile elements would be held in sulfide phases dispersed in the solidified magma chamber and would not be available to partition into the volatile phase. The Boggy Plain zoned pluton, Australia provides an example of a barren magmatic system in which >87% of the Cu, and possibly more Au and platinum group elements (PGE: Pd, Pt, Rh, Ru and Ir), is held in dispersed Cu-rich sulfide blebs trapped in silicate minerals (Park *et al.*, 2013*b*). Therefore, investigation of the sulfide saturation history in evolving magmas provides important information for evaluating the potential of the magmatic system to form a magmatic–hydrothermal Cu–Au ore deposit. Recent studies on the PGE geochemistry of intermediate–felsic rocks (Park *et al.*, 2013*a*, 2013*b*) have shown that the variation of these elements, along with Cu and Au, can be used as a sensitive indicator of sulfide saturation in an evolving magmatic system. The abundances of all PGE, and the Pd/Cu ratio of the melt, decrease significantly when an immiscible sulfide melt starts to segregate from a magma.

The lavas from the Niuatahi–Motutahi volcano (Niuatahi and Motutahi are Tongan names for the caldera and central cone, respectively) from the Tonga rear arc are submarine volcanic rocks that erupted ~1700 m below sea level. Copper- and Au-rich native sulfur mineralization occurs in association with the Niuatahi–Motutahi lavas and the metals and sulfur are considered to have originated from the Niuatahi–Motutahi magma (Kim *et al.*, 2011). Therefore, the Niuatahi–Motutahi lavas and native sulfur provide an example of metal transport by a volatile phase from a magmatic system below to a hydrothermal system above. We present the results of whole-rock major and trace element analyses, including PGE, Au and Re data, for the Niuatahi–Motutahi lavas. Whole-rock, mineral, glass and melt inclusion analyses are used to investigate the relative timing of sulfide and volatile saturation and the behavior of chalcophile elements during sulfide- and volatile-saturated magmatic differentiation. We use these data to show that late sulfide saturation in the Niuatahi–Motutahi lavas resulted in the magmas being enriched in Cu and Au at the time of volatile exsolution, which led to the formation of Cu–Au-rich native sulfur mineralization.

GEOLOGICAL SETTING AND SAMPLE LOCATION

The Niuatahi–Motutahi caldera, also known as Volcano O (Arculus, 2005) and MTJ-1 (Kim *et al.*, 2009), is a rear arc volcanic complex located in the NE Lau Basin, SW Pacific Ocean (Fig. 1). The NE Lau Basin lies within a crustal extension zone between the Tonga arc and the NE Lau Basin spreading center (NELSC) (Zellmer & Taylor, 2001). Owing to its unique tectonic setting, the NE Lau Basin hosts various types of submarine volcanism produced by a combination of subduction-associated water-fluxed melting and crustal extension (Resing *et al.*, 2011, and references therein). The geochemical features of the lavas from the NE Lau Basin vary from mid-ocean ridge basalt (MORB)-like (e.g. Mangatolu Triple Junction) to arc-like (e.g. Fonualei spreading center) (Keller *et al.*, 2008).

Submarine lava samples used in this study were collected from the Niuatahi–Motutahi caldera and a separate volcanic region located ~5 km SE of the caldera during the Korea Deep Ocean Study (KODOS) H-06 cruise (Fig. 1c). They were dredged at water depths that range from 1300 to 1900 m. Strong hydrothermal signals detected near the cone of the caldera and sparse sediment cover (Kim *et al.*, 2009) indicate that the volcano has been active until recently. Native sulfur

Downloaded from http://petrology.oxfordjournals.org/ by guest on January 20, 2015

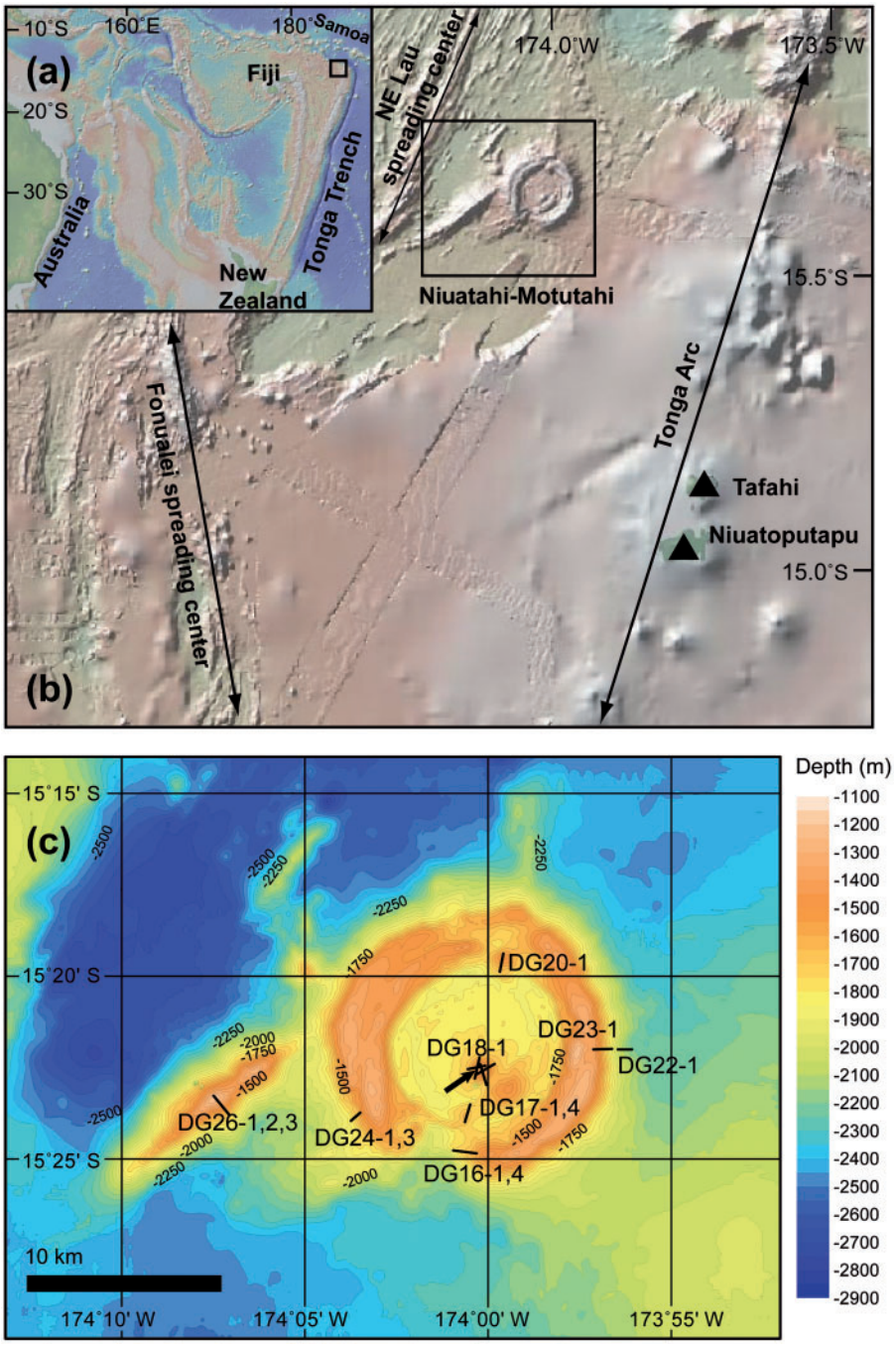

Fig. 1. Location maps for the Niuatahi–Motutahi volcano. (a) Regional map showing the location of the Tonga Trench, north of New Zealand. The square represents the NE Lau Basin area. (b) Map of the NE Lau Basin. (c) Seafloor bathymetry and sample dredge sites for the Niuatahi–Motutahi volcano (after Kim *et al.*, 2009). The arrow represents the location of native sulfur and active hydrothermal vent sites.

mineralization occurs in association with dacite in the volcanic cone of the active caldera (Fig. 1c). It is a potential target for the Korea Institute of Ocean Science and Technology for submarine mineral exploration. The mineralization contains about 1·8% of Cu, 1·7 g t^{-1} of Au and 0·9 g t^{-1} of Ag (Kim *et al.*, 2011). The occurrence of numerous poorly crystallized covellite inclusions in the sulfur matrix and the low whole-rock sulfur isotopic composition ($\delta^{34}S = -7{\cdot}5‰$ to $-8{\cdot}2‰$) indicate that the metal-bearing native sulfur is a condensate produced from a sulfur-rich magmatic vapor exsolved by the Niuatahi–Motutahi magma (Kim *et al.*, 2011).

ANALYTICAL TECHNIQUES

Electron microprobe analyses

The major element compositions of silicate, oxide and sulfide minerals, melt inclusions and glasses were

Downloaded from http://petrology.oxfordjournals.org/ by guest on January 20, 2015

measured by a CAMECA EX100 electron microprobe at the Australian National University (ANU), operated at 15 kV with a 20 nA beam current. A beam size of 1 μm was used for mineral analyses but the beam was defocused to 5 μm and 10 μm for analyses of melt inclusions and glasses. The CAMECA set of synthetic and natural minerals and USGS VG-2 glass were used as standards. The 2σ analytical error, obtained from replicate measurements ($n = 13$) of the USGS VG-2 glass standard, was 0·7% for SiO_2, 1·1% for MgO and CaO, 1·5% for TiO_2, 0·8% for Al_2O_3 and FeO, 6·6% for Na_2O, and 19% for P_2O_5 and MnO, with all errors expressed as a percentage of the element concentration (Supplementary Data A; supplementary data are available for downloading at http://www.petrology.oxfordjournals.org). Detection limits for Cl and S were ~200 ppm and the analytical 2σ errors were 11% and 14% respectively.

LA-ICP-MS analyses

Trace element concentrations in glasses and a sulfide were measured by laser ablation inductively coupled plasma mass spectrometry (LA-ICP-MS) at the ANU. The system is composed of a Lambda Physik COMPex 110 excimer laser (λ = 193 nm), ANU-designed HelEx ablation cell, and an Agilent 7700 ICP-MS system. The analyses were carried out using spot sizes that varied between 81 and 105 μm and a laser pulse rate of 5 Hz. Each analysis consists of 25 s of background measurement and 40 s of sample ablation. NIST 610 glass (Jochum *et al.*, 2011) was used as the primary standard for trace elements and CANMET po727 FeS (Fonseca, 2007) was used for the PGE. To correct for yield differences between standards and unknown samples, ^{43}Ca and ^{57}Fe, measured by electron microprobe, were used for the trace element and PGE data reduction, respectively. Gold contents of the microcrystalline groundmass of the rocks and glasses were measured using NIST 610 glass with ^{29}Si as the internal standard.

Data reduction was performed using the Iolite software package (Paton *et al.*, 2011) for trace elements, and an in-house Excel spreadsheet for the PGE using the relationship described by Longerich *et al.* (1996) and Sylvester & Eggins (1997). The isotopes used to determine the concentrations are as follows: ^{29}Si, ^{31}P, ^{43}Ca, ^{45}Sc, ^{49}Ti, ^{51}V, ^{53}Cr, ^{55}Mn, ^{57}Fe, ^{59}Co, ^{60}Ni, ^{61}Ni, ^{65}Cu, ^{66}Zn, ^{85}Rb, ^{89}Y, ^{90}Zr, ^{93}Nb, ^{108}Pd, ^{111}Cd, ^{133}Cs, ^{137}Ba, ^{139}La, ^{140}Ce, ^{141}Pr, ^{146}Nd, ^{147}Sm, ^{153}Eu, ^{157}Gd, ^{159}Tb, ^{163}Dy, ^{165}Ho, ^{166}Er, ^{169}Tm, ^{172}Yb, ^{175}Lu, ^{178}Hf, ^{181}Ta, ^{195}Pt, ^{197}Au, ^{208}Pb, ^{232}Th, ^{238}U. For the PGE analysis isobaric interferences by metal oxides and metal argides were corrected according to the method described by Park *et al.* (2012*a*) using sphalerite and R33 zircon. The correction assumes that blank-corrected signals of ^{108}Pd in sphalerite and R33 zircon result from argide or oxide interferences. The isobaric interferences by $^{68}Zn^{40}Ar^{+}$ and $^{92}Zr^{16}O^{+}$ at ^{108}Pd were corrected and the corrections were 30–50% for glasses and ~20% for sulfides. The detection limits for Pd, Pt and Au were 3 ppb, 6 ppb and 1–2 ppb respectively. Multiple analyses of BCR-2 g were carried out to check the accuracy and precision of the analyses, and the results agree with reported values (Supplementary Data A).

Whole-rock major and trace element analyses

Prior to whole-rock analysis samples were crushed, sonicated in distilled water and dried. Crushed fragments were hand-picked under a microscope to exclude altered particles. Before final grinding, samples were leached in 1 M HCl for 10 min at room temperature. Major and trace elements for 12 samples were determined by a combination of inductively coupled plasma atomic emission spectrometry (ICP-AES) and ICP-MS analysis (4LithoResearch) by Activation Laboratories, Canada. Samples were prepared and analyzed in a batch system. Each batch contains a method reagent blank, certified reference material and 17% replicates ($n = 4$). Samples were mixed with a flux of lithium metaborate and lithium tetraborate and fused in an induction furnace. The melt was immediately poured into a solution of 5% nitric acid containing an internal standard, and mixed continuously until completely dissolved (~30 min). The samples were analyzed for major oxides and selected trace elements on a combination simultaneous–sequential ICP-AES (Thermo Jarrell–Ash ENVIRO II) and ICP-MS (Perkin–Elmer ELAN 6000) system. Calibration was performed using seven prepared USGS and CANMET certified reference materials. One of the seven standards was used during the analysis for every group of 10 samples. The uncertainty on the external reproducibility of the analyses was within ±5 relative %. Major and trace element data for an additional three samples were measured by X-ray fluorescence (XRF) (Bruker S8 Tiger) and ferrous iron concentrations for five samples were measured by the titration method at Geoscience Australia.

Whole-rock PGE and RE analyses

Whole-rock PGE and Re concentrations in the Niuatahi–Motutahi lavas were measured using the Ni-sulfide fire assay-isotope dilution method described by Park *et al.* (2012*b*). Briefly, ~300 g of fresh rock fragments collected from each sample were ground to a fine powder in an agate mill. A 5 g split of this powder was thoroughly mixed with 0·5 g of Ni, 0·25 g of S and 5 g of sodium borax, and an enriched PGE spike solution (^{99}Ru, ^{105}Pd, ^{185}Re, ^{191}Ir and ^{195}Pt) was added to the mixture. The spiked powder was dried at 100°C for 60 min and fused in a preheated open furnace at 1100°C for 30 min. Nitrogen gas was introduced into the furnace at a flow rate of ~0·03 $m^3 min^{-1}$ and a second outside crucible, containing ~0·1 g of flour, was used to provide reducing conditions during fusion. After quenching, Ni-sulfide beads were collected and dissolved in 6 M HCl. The solution was then filtered through a Millipore filter paper (0·45 μm cellulose membrane) to collect the PGE-bearing minerals. The

Downloaded from http://petrology.oxfordjournals.org/ by guest on January 20, 2015

filter paper containing the PGE minerals was then digested in aqua regia. After complete digestion, the solutions were dried down to ~100 μl and diluted with 2% HNO_3.

An Agilent 7700 x quadrupole ICP-MS system at the ANU was used to measure the PGE and Re isotopes. The sensitivities in each analysis were 2·4 to $3{\cdot}4 \times 10^5$ c.p.s. ppb^{-1} for masses 89, 140 and 205. Potential molecular interferences on the analyzed isotopes by Ni, Cu, Zn, Co, Hf, Mo, Zr and Ta argides or oxides were monitored and the effects of the interferences were subtracted using measured oxide and argide production rates. Argide production rates were 0·003–0·006% and oxide production rates 0·2–0·3%. The interference correction is <0·2% for all PGE and Re, except for Ru for which the correction is 2–13%. Concentrations of Ir, Ru, Pt, Pd and Re were determined by isotope dilution using the $^{191}Ir/^{193}Ir$, $^{99}Ru/^{101}Ru$, $^{191}Ir/^{193}Ir$, $^{195}Pt/^{194}Pt$, $^{105}Pd/^{108}Pd$ and $^{185}Re/^{187}Re$ ratios, respectively. Concentrations of Rh were obtained using the method described by Meisel *et al.* (2003) and Park *et al.* (2012*b*), which uses the count rates of ^{103}Rh and ^{106}Pd, assuming that the loss of Rh during the analytical procedure was similar to the loss of Pd.

Average procedural blanks determined by sample-free analyses ($n = 5$) were 0·8 ± 0·1 ppt for Ir, 2·1 ± 0·4 ppt for Ru, 0·8 ± 0·2 ppt for Rh, 16 ± 9 ppt for Pt, 17 ± 4 ppt for Pd, and 18 ± 2 ppt for Re. The method detection limits (MDL), taken to be three standard deviations of the procedural blanks after subtraction of average procedural blank values, were 0·3 ppt for Ir, 1·2 ppt for Ru, 0·5 ppt for Rh, 26 ppt for Pt, 11 ppt for Pd, and 5 ppt for Re. To assess the accuracy and precision of the analyses we performed replicate analyses of the reference material TDB-1. The reproducibilities for Pd and Pt were 2% and 6% respectively, and 9–14% for the other PGE and Re. The reported values are consistent with those of Peucker-Ehrenbrink *et al.* (2003) and Meisel & Moser (2004) to within 2σ error (Supplementary Data A) although our Re value of ~0·72 ppb is slightly lower than the ~1 ppb reported by Ishikawa *et al.* (2014).

RESULTS

Petrography and mineralogy of the Niuatahi–Motutahi lavas

The lavas from the volcanic cone and ring-shaped wall of the Niuatahi–Motutahi caldera are aphyric to porphyritic dacites that consist dominantly of a microcrystalline or glassy groundmass containing small amounts (<5 modal %) of plagioclase, augite, and pigeonite phenocrysts with minor magnetite (Fig. 2a; see Supplementary Data A for mineral compositions). Homogeneously distributed, elongate vesicles characterize the dacites. The pigeonite, augite and plagioclase phenocrysts are euhedral to subhedral and range from 200 to 800 μm in size. Ti-rich magnetite and melt inclusions are commonly trapped in the phenocrysts (Fig. 2c). Pigeonite and augite phenocrysts have Mg# in the range of 55–68 and 58–70, respectively [$Mg\# = 100X_{Mg}/(X_{Mg} + X_{Fe})$]. They show limited Mg# variations within a sample (typically <4) and the variation is highest in the least evolved dacites and decreases with increasing SiO_2 content of the host rocks. These compositions are in equilibrium with the host rock composition (Mg# = 27–41), assuming a Mg–Fe partition coefficient (K_D) of 0·29 ± 0·06 for pigeonite and 0·28 ± 0·08 for augite (Putirka, 2008). Plagioclase crystals have anorthite contents (An) that vary between 92 and 96 mol % and correlate negatively with the SiO_2 contents of host rocks. An elliptical magmatic sulfide bleb, with a diameter of ~20 μm (Fig. 2e and Supplementary Data B), was found in the glassy matrix of one dacite sample (DG24-3). It contains 26–35 wt % Cu and 31–38 wt % Fe and plots in the liquid field on the Cu–Fe–S phase diagram at 1000°C (Fig. 3). The observed compositional variation is consistent with the sulfide bleb consisting of several phases. The experimental investigation by Ebel & Naldrett (1997) of the phase relations in the Cu–Fe–S system at 1000°C showed that Cu-rich sulfide liquid coexists with monosulfide solid solution (MSS), intermediate solid solution (ISS) and bornite that are exsolved from the liquid during quenching. The composition of the sulfide bleb in the dacite is comparable with the results of the Ebel & Naldrett (1997) experiments and varies along the line between bornite, ISS and MSS (Fig. 3), which suggests that the measured sulfide composition represents a mixture of these three phases. The shape and composition of the sulfide bleb indicate that it was trapped as a liquid phase and quenched at >1000°C before experiencing low-temperature recrystallization.

Lavas collected from the volcanic complex SE of the Niuatahi–Motutahi caldera are olivine- and clinopyroxene-bearing basalts. They are composed of a microcrystalline groundmass with varying amounts of olivine and clinopyroxene phenocrysts (~20–40 modal %), and minor plagioclase and Cr spinel (Fig. 2b; see Supplementary Data A for mineral compositions). Andesitic vesicle-filling glasses occur in one sample (Fig. 2f); these are interpreted to form when residual melt flows into early formed vesicles (Smith, 1967; Upton & Wadsworth, 1971). Upton & Wadsworth (1971) suggested that residual melt is 'segregated into the partly vacated vesicle cavities by a process of suction towards low-pressure sites, and there congealed as a glass'. The olivine and clinopyroxene crystals are euhedral to subhedral and range in size from 300 μm to 2 mm. The Fo contents of the cores of olivine phenocrysts vary between Fo_{81} and Fo_{89} with variations within a single sample typically <5 mol %. Olivine crystals are rarely zoned, but some large crystals (>800 μm) show normal zoning with their cores having Fo contents that are two or three units higher than their rims. The high-Fo olivines ($Fo_{86–89}$) would have been in equilibrium with parental magmas containing about 8–11 wt % MgO, assuming an Mg–Fe partition coefficient (K_D) of 0·3 ± 0·04. This suggests that some basalt samples with high MgO contents (>12 wt %) resulted from

Downloaded from http://petrology.oxfordjournals.org/ by guest on January 20, 2015

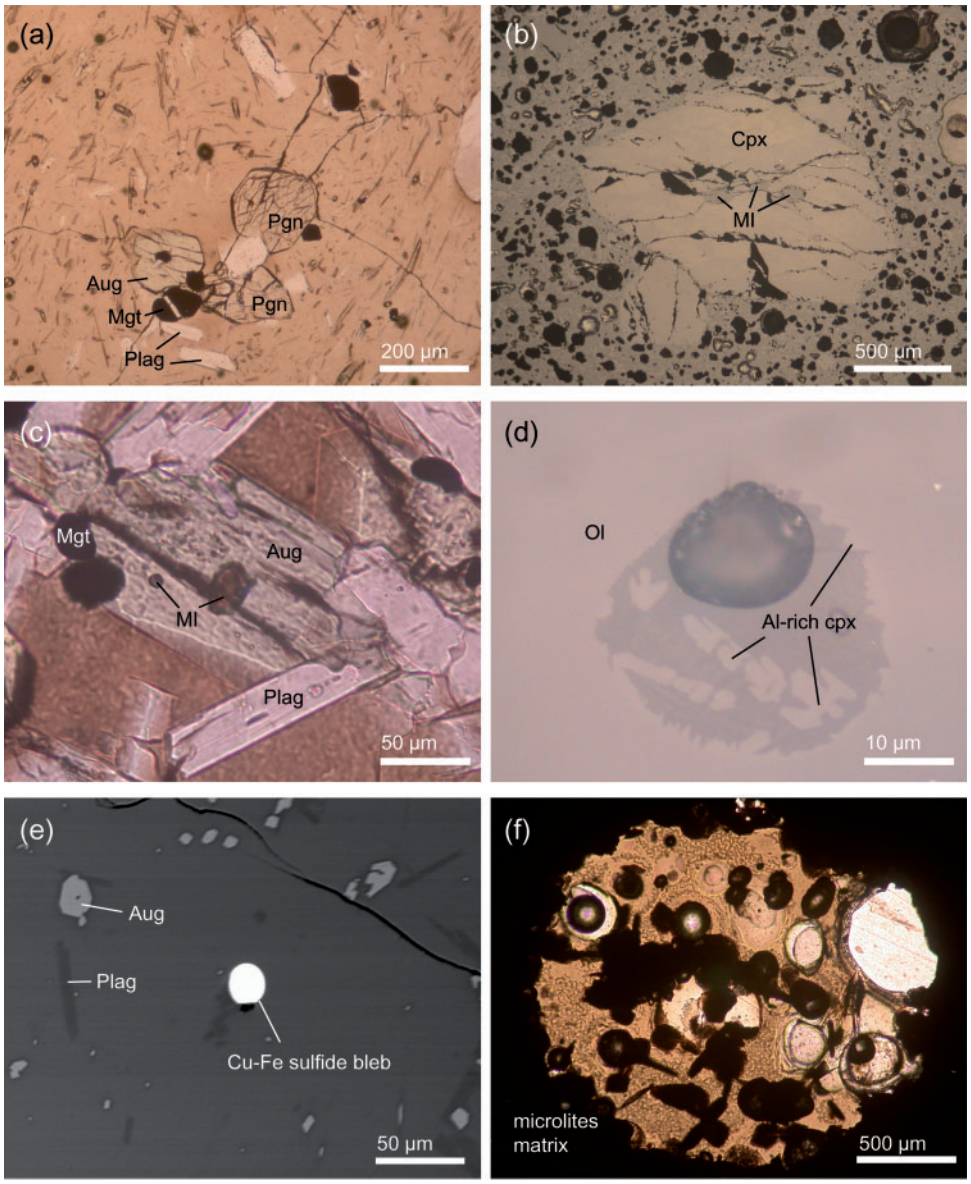

Fig. 2. Optical and back-scattered electron images of Niuatahi–Motutahi lavas. (a) Pigeonite, augite, plagioclase and magnetite crystals in glassy matrix of the low-K dacite (DG24-3). (b) Clinopyroxene phenocryst in a basalt with a micro-crystalline groundmass containing various sizes of vesicles (DG26-3). Melt inclusions (MI) are trapped in the core of the clinopyroxene. (c) Dacitic melt inclusions hosted by an augite crystal from the low-K dacite (DG24-3). (d) Melt inclusion in olivine from a basalt (DG26-1) that contains abundant skeletal Al-rich clinopyroxene grains, which formed during quenching, and a vapor bubble. This type of melt inclusion was not used for post-entrapment crystallization correction. (e) Cu–Fe sulfide bleb trapped in a glassy matrix from a low-K dacite (DG24-3). (f) Vesicle-filling glass from a basalt (DG26-2).

accumulation of olivine phenocrysts. Clinopyroxene phenocrysts have Mg# of 80–88. Like olivine, the Mg# variation in clinopyroxene within single samples is <5 mol %. Cr spinels mostly occur as 5–50 µm sized inclusions within olivine or clinopyroxene and have Cr# [$Cr\# = 100X_{Cr}/(X_{Cr} + X_{Al})$] ranging from 72 to 84, except for one sample, DG26-3, which has relatively low Cr# ranging from 55 to 62.

Whole-rock major and trace element geochemistry

Whole-rock analyses of the Niuatahi–Motutahi lavas plot in the fields of basalt, basaltic andesite and dacite in a total alkalis–silica diagram (Fig. 4; Table 1). The vesicle-filling glass from the basalt is andesitic and the dacite glasses are identical in composition to their host rocks (Fig. 4). Most samples plot on the boundary between medium- and low-K series (island arc tholeiite series) on a K_2O vs silica diagram, and follow a trend similar to that of the other Tonga arc lavas (Fig. 4). The tholeiitic index (THI; Zimmer *et al.*, 2010), calculated using the Fe contents of Niuatahi–Motutahi basalts (7 wt % < MgO < 9 wt %) and the vesicle-filling glasses (3 wt % < MgO < 5 wt %), is 0·94, which indicates a moderate Fe depletion trend. This suggests that the lavas are slightly more calc-alkaline than tholeiitic. This value is

Downloaded from http://petrology.oxfordjournals.org/ by guest on January 20, 2015

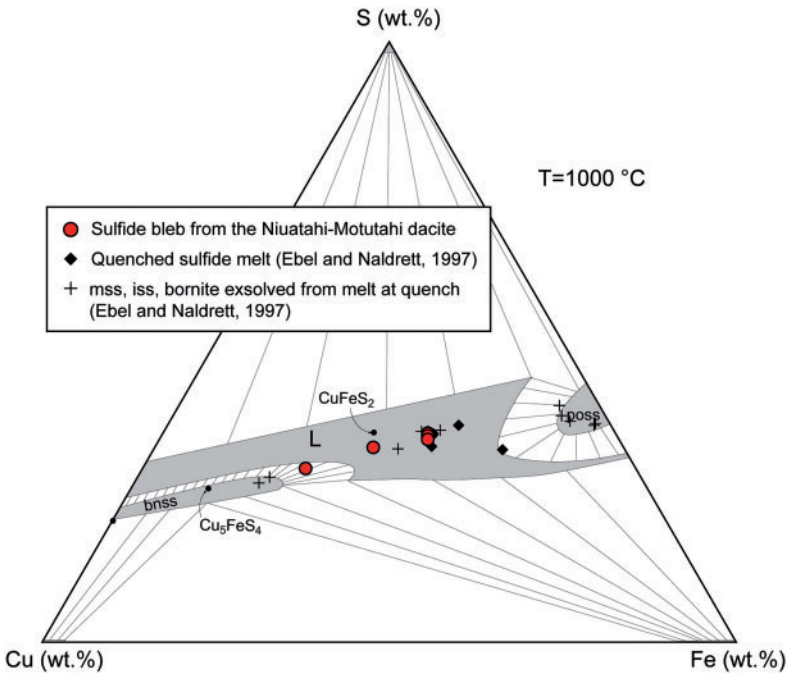

Fig. 3. Phase relations in the Cu–Fe–S system at 1000°C, modified from Kullerud *et al.* (1966), for a sulfide bleb from the Niuatahi–Motutahi dacite. The composition of quenched sulfide melt and MSS, ISS and bornite exsolved from the melt from the experimental study of Ebel & Naldrett (1997) are shown for comparison. L, liquid; bnss, bornite solid solution; poss, pyrrhotite solid solution; mss, monosulfide solid solution; iss, intermediate solid solution.

similar to that of arc lavas (THI < 1; Zimmer *et al.*, 2010) and is distinct from those of typical back-arc basin lavas (1·2 < THI < 1·8; Zimmer *et al.*, 2010).

Major element variations plotted against the MgO content of the lavas are consistent with fractional crystallization trends of transitional calc-alkaline magmas (Fig. 5; Table 1). The high MgO contents (>12 wt % MgO) of two basalt samples can be attributed to olivine accumulation (Fig. 5a). The decrease in Al_2O_3 and CaO below ~5 wt % MgO reflects plagioclase becoming the dominant crystallizing mineral. FeO and TiO_2 decrease significantly below 3 wt % MgO, suggesting the onset of Ti-bearing magnetite crystallization (Fig. 5d and f). Variations in trace elements correspond to those of the major elements (Fig. 6; Table 1). The continuous decrease of Sc reflects fractional crystallization of clinopyroxene from the basalts and dacites. Vanadium and Sr reach their maximum abundances at ~5 wt % MgO and progressively decrease in dacite, corresponding to the onset of magnetite and plagioclase crystallization, respectively. The major and trace element variations are consistent with the occurrence and abundance of the phenocryst mineral assemblages. However, it should be noted that three samples (DG17-4, DG17-1, DG20-1; shown as light-coloured diamonds in Fig. 4) have higher K_2O than the majority of the dacites (Fig. 4b). They are also enriched in large ion lithophile elements [LILE; Ba, Rb, Cs, light rare earth elements (LREE)] and some refractory elements such as Hf, Zr and Ta (Fig. 6 and Table 1) compared with the other dacites. Therefore, the Niuatahi–Motutahi dacites can be subdivided into two

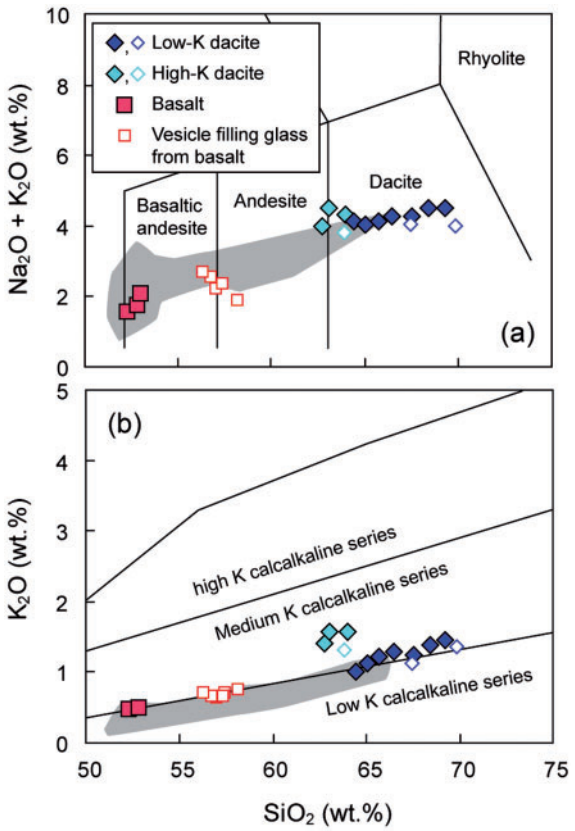

Fig. 4. (a, b) Total alkalis vs silica (TAS) diagram and K_2O vs silica diagram (after Le Maitre *et al.*, 1984). Open and filled diamonds represent dacite glasses and whole-rock dacite, respectively. The grey field represents the compositions of Tonga arc volcanic rocks (GEOROC database http://www.georoc.mpch-mainz.gwdg.de).

Downloaded from http://petrology.oxfordjournals.org/ by guest on January 20, 2015

Table 1: Major and trace element compositions of the Niuatahi–Motutahi lavas

Rock type:	Basalt			Vesicle-filling glass						High-K dacite				Low-K dacite								
Locality:	SW branch			SW branch						N–M				N–M								
Sample:	DG26-1	DG26-2	DG26-3	DG26-2-VFG-1*	DG26-2-VFG-2*	DG26-2-VFG-3*	DG26-2-VFG-4*	DG26-2-VFG-5*	DG26-2-VFG-6*	DG17-4	DG17-4g	DG17-1	DG20-1	DG18-1	DG24-1	DG24-3	DG24-3g	DG23-1	DG16-4	DG22-1	DG22-1g*	DG16-1
Depth (m):	1600	1600	1600	1600	1600	1600	1600	1600	1600	1757	1757	1757	1699	1629	1803	1803	1803	1668	1785	2190	2190	1785
Major element																						
SiO_2	52·3	52·9	53·0	57·0	57·4	56·7	57·4	58·2	56·3	62·8	63·9	63·98	63·1	64·4	65·0	65·7	67·4	66·5	67·5	68·4	69·9	69·3
TiO_2	0·34	0·36	0·47	0·49	0·45	0·51	0·46	0·50	0·47	0·62	0·61	0·57	0·64	0·57	0·56	0·56	0·56	0·56	0·57	0·52	0·51	0·48
Al_2O_3	11·5	12·3	15·8	15·6	16·0	16·0	16·2	16·2	16·3	13·7	13·8	13·37	13·4	13·2	12·6	12·7	13·1	12·7	12·5	12·6	12·4	12·5
Fe_2O_3	1·19	9·10	1·45	9·43	9·67	9·21	9·18	9·69	9·72	2·47	8·87	7·11	1·37	8·17	7·99	1·27	7·95	7·46	1·28	6·92	6·98	0·95
FeO	7·27	n.d.	7·77	n.d.	n.d.	n.d.	n.d.	n.d.	n.d.	5·85	n.d.	n.d.	5·95	n.d.	n.d.	6·04	n.d.	n.d.	5·72	n.d.	n.d.	4·65
MnO	0·16	0·16	0·17	n.d.	0·20	0·20	n.d.	0·20	0·20	0·14	0·13	0·11	0·14	0·13	0·16	0·16	0·15	0·14	0·15	0·14	0·13	0·12
MgO	14·3	12·8	7·27	5·15	5·29	5·46	4·75	4·18	4·69	2·24	2·13	2·24	1·73	1·69	1·37	1·38	1·35	1·24	1·15	1·09	0·89	0·98
CaO	9·87	10·3	10·9	11·0	11·0	11·0	10·9	9·4	10·0	6·53	6·30	5·91	5·66	5·73	5·31	5·32	5·20	5·10	4·91	4·65	4·45	4·34
Na_2O	1·11	1·25	1·34	1·57	1·65	1·85	1·71	1·12	2·01	2·58	2·50	2·72	2·92	3·12	2·93	2·93	2·93	2·98	3·04	3·13	2·63	3·08
K_2O	0·46	0·50	0·73	0·64	0·70	0·67	0·65	0·75	0·69	1·41	1·31	1·58	1·57	1·02	1·13	1·21	1·12	1·30	1·25	1·38	1·35	1·45
P_2O_5	0·09	0·09	0·14	n.d.	0·13	0·13	n.d.	0·14	0·13	0·22	0·24	0·23	0·25	0·22	0·21	0·21	0·22	0·23	0·23	0·21	0·21	0·18
LOI	0·08	0·06	n.d.	n.d.	n.d.	n.d.	n.d.	n.d.	n.d.	0·79	n.d.	2·44	2·34	0·38	1·29	1·03	n.d.	1·02	0·95	1·28	n.d.	1·09
Total	99·5	99·7	99·1	100·8	102·5	101·8	101·2	100·4	100·5	100·0	99·8	100·30	99·7	98·6	98·6	99·2	100·0	99·2	99·9	100·4	99·4	99·7
Trace element†																						
S	n.d.	n.d.	n.d.	<250	<250	<250	<250	<250	<250	n.d.	<250	n.d.	n.d.	n.d.	n.d.	n.d.	<250	n.d.	n.d.	n.d.	<250	n.d.
Cl	n.d.	n.d.	n.d.	1260	1242	1098	1283	1485	1321	n.d.	2966	n.d.	n.d.	n.d.	n.d.	n.d.	2949	n.d.	n.d.	n.d.	2637	n.d.
Sc	42·0	43·0	38·2	n.d.	37·1	38·9	36·8	34·0	35·8	28·0	25·9	23·0	24·0	25·0	26·0	26·0	21·8	23·0	24·0	22·0	21·5	20·0
V	239	252	333	n.d.	301	303	289	308	293	277	248	203	192	196	123	120	83	101	86	74	52	56
Cr	810	660	169	n.d.	37	41	48	20	30	<20	0·45	40	20	<20	<20	<20	0·16	<20	<20	<20	0·35	<20
Co	52·0	43·0	35·7	n.d.	28·3	28·7	27·0	27·9	28·1	20·0	18·7	16·0	16·0	16·0	14·0	15·0	12·2	12·0	12·0	11·0	10·9	9·0
Ni	240	190	93	n.d.	23	26	21	17	20	<20	2·98	<20	<20	<20	<20	<20	0·39	<20	<20	<20	0·67	<20
Cu	90	80	120	n.d.	199	193	185	231	234	200	201	160	150	130	120	130	123	100	110	100	102	80
Zn	70	60	67	n.d.	70·02	66·54	71·11	72·88	70·68	90	76	90	90	80	100	100	86	90	100	100	81	90
Cs	0·50	0·20	0·37	n.d.	0·27	0·26	0·28	0·30	0·27	0·60	0·60	0·70	0·60	0·30	0·50	0·50	0·50	0·50	0·50	0·60	0·59	0·60
Rb	9·0	8·0	5·0	n.d.	12·5	11·8	12·5	13·9	12·4	23·0	26·3	26·0	24·0	16·0	19·0	20·0	21·2	22·0	21·0	25·0	25·4	26·0
Sr	172	183	253	n.d.	268	264	271	274	258	263	262	242	278	250	259	260	257	265	263	254	237	249
Ba	99	104	114	n.d.	153	145	150	170	151	290	281	311	305	243	257	268	288	295	282	306	297	319
Nb	1·40	1·30	1·34	n.d.	2·38	2·22	2·36	2·56	2·29	5·48	7·84	7·23	7·48	5·82	5·99	5·94	6·26	6·72	6·37	6·43	6·43	6·63
Ta	0·07	0·07	0·06	n.d.	0·10	0·10	0·11	0·11	0·10	0·40	0·40	0·41	0·46	0·32	0·34	0·32	0·32	0·36	0·35	0·34	0·31	0·39
Zr	17·0	19·0	21·3	n.d.	28·0	27·6	27·6	30·4	27·4	51·0	58·1	54	56·0	49·0	49·0	50·0	54·4	53·0	52·0	52·0	57·8	57·0
Y	8·30	8·10	9·46	n.d.	10·8	11·0	10·7	11·7	10·8	15·8	17·0	16·9	18·0	18·6	18·4	18·9	19·1	18·5	19·7	19·1	19·6	20·0
La	3·82	3·73	4·45	n.d.	5·53	5·32	5·40	6·17	5·44	9·8	11·4	11·0	11·8	10·0	10·5	10·0	10·1	11·0	10·7	11·1	10·7	10·8
Ce	7·72	7·79	9·56	n.d.	11·5	10·9	10·9	12·5	11·1	20·3	23·5	22·4	23·7	19·9	21·0	20·1	21·3	22·1	21·6	22·6	22·4	22·3
Pr	0·96	0·96	1·34	n.d.	1·45	1·39	1·42	1·60	1·43	2·59	2·91	2·77	3·02	2·56	2·70	2·59	2·67	2·85	2·78	2·75	2·81	2·76
Nd	4·29	4·30	6·24	n.d.	6·40	6·22	6·48	7·14	6·42	11·7	12·5	12·0	13·6	11·5	11·9	11·4	11·8	12·3	11·9	11·9	12·1	12·2
Sm	1·03	1·11	1·56	n.d.	1·57	1·58	1·59	1·75	1·56	2·73	2·83	2·82	3·04	2·80	2·87	2·82	2·85	2·96	3·05	2·78	2·98	2·96
Eu	0·43	0·44	0·54	n.d.	0·58	0·58	0·57	0·62	0·58	0·85	0·84	0·79	0·95	0·86	0·86	0·84	0·88	0·91	0·91	0·94	0·87	0·84
Gd	1·18	1·20	1·58	n.d.	1·72	1·70	1·72	1·83	1·68	3·06	2·89	2·81	3·32	3·00	3·17	3·06	3·07	3·16	3·21	3·05	3·17	3·06
Tb	0·22	0·22	0·26	n.d.	0·28	0·26	0·26	0·30	0·27	0·50	0·43	0·43	0·50	0·48	0·51	0·49	0·48	0·51	0·51	0·53	0·50	0·49
Dy	1·41	1·45	1·79	n.d.	1·83	1·83	1·87	1·94	1·77	3·20	2·86	2·82	3·38	3·25	3·38	3·24	3·19	3·33	3·32	3·28	3·33	3·19
Ho	0·29	0·31	0·38	n.d.	0·39	0·39	0·38	0·42	0·38	0·69	0·58	0·61	0·71	0·69	0·74	0·69	0·67	0·68	0·72	0·67	0·68	0·67
Er	0·90	0·96	1·09	n.d.	1·21	1·22	1·18	1·24	1·18	2·22	1·86	1·86	2·25	2·20	2·27	2·12	2·10	2·22	2·19	2·07	2·17	2·13
Tm	0·14	0·15	n.d.	0·18	0·17	0·17	0·18	0·17	0·31	0·28	0·25	0·32	0·31	0·32	0·29	0·31	0·31	0·32	0·33	0·31	0·32	
Yb	0·97	1·00	1·03	n.d.	1·29	1·30	1·25	1·37	1·25	2·19	1·88	1·93	2·22	2·21	2·29	2·17	2·19	2·24	2·20	2·26	2·25	2·23
Lu	0·15	0·15	0·17	n.d.	0·19	0·18	0·20	0·21	0·18	0·36	0·30	0·30	0·36	0·36	0·37	0·35	0·34	0·35	0·36	0·34	0·35	0·36
Hf	0·60	0·60	0·58	n.d.	0·75	0·73	0·76	0·80	0·72	1·60	1·66	1·70	1·80	1·60	1·50	1·50	1·57	1·50	1·60	1·60	1·69	1·80
Th	0·53	0·54	0·42	n.d.	0·84	0·80	0·83	0·92	0·82	1·52	1·72	1·62	1·64	1·50	1·40	1·46	1·57	1·54	1·55	1·55	1·65	1·67
U	0·22	0·20	0·27	n.d.	0·31	0·30	0·31	0·34	0·30	0·52	0·62	0·58	0·66	0·56	0·51	0·52	0·60	0·55	0·55	0·57	0·65	0·60

Downloaded from http://petrology.oxfordjournals.org/ by guest on January 20, 2015

Table 1. (continued)

Rock type:	Basalt			Vesicle-filling glass							High-K dacite					Low-K dacite							
Locality:	SW branch			SW branch							N–M					N–M							
Sample:	DG26-1	DG26-2	DG26-3	DG26-2-VFG-1*	DG26-2-VFG-2*	DG26-2-VFG-3*	DG26-2-VFG-4*	DG26-2-VFG-5*	DG26-2-VFG-6*	DG17-4	DG17-4g	DG17-1	DG20-1	DG18-1	DG24-1	DG24-3	DG24-3g	DG23-1	DG16-4	DG22-1	DG22-1g*	DG16-1
Depth (m):	1600	1600	1600	1600	1600	1600	1600	1600	1600	1757	1757	1757	1699	1629	1803	1803	1803	1668	1785	2190	2190	1785
Pb	n.d.	n.d.	2·01	n.d.	2·44	2·24	2·53	2·89	2·43	3·04	4·56	4·08	3·68	3·03	3·52	3·41	4·14	3·61	3·63	n.d.	4·62	3·98
Au‡	n.d.	5·4	6·1	n.d.	5·9	4·7	n.d.	6·9	6·6	6·7	5·5	6·4	n.d.	5·3	5·9	3·6	2·4	2·8	1·4	n.d.	<1	<2
ΔQFM log fO_2§										1·90			0·65			0·50			0·40			0·40

Major elements are in wt %, trace elements are in ppm, and Au is in ppb. LOI, loss on ignition; n.d., not determined. Major and trace elements were measured by a combination of ICP-AES and ICP-MS unless otherwise mentioned. N–M, Niuatahi–Motutahi.

*Major elements were analyzed by electron microprobe analysis, trace elements by LA-ICP-MS.

†Sr, Nb, Pb and REE were analyzed by LA-ICP-MS.

‡Average Au concentrations of glassy matrix or microcrystalline groundmass measured by LA-ICP-MS. Raw data are provide in Supplementary Data A.

§Calculated using Fe^{3+}/Fe^{2+} measured by titration.

groups, a low-K group and a high-K group, based on their geochemistry (Figs 4 and 6).

The MORB-normalized incompatible trace element patterns of the Niuatahi–Motutahi lavas are characterized by enrichment of LILE relative to high field strength elements (HFSE) and REE, with pronounced negative Nb and Ta anomalies relative to adjacent elements (Fig. 7). These geochemical features are typical of island arc lavas (Pearce & Stern, 2006), indicating a significant input of a subduction component into the mantle source of the Niuatahi–Motutahi lavas. The trace element patterns of the Niuatahi–Motutahi lavas, particularly the mafic ones, are similar to those of neighboring Tonga arc volcanoes, Tafahi and Niuatoputapu (Fig. 7). The trace elements patterns are subparallel for all rock types, suggesting a comagmatic origin of the Niuatahi–Motutahi lavas. The dacites show pronounced negative Ti anomalies owing to Ti-magnetite crystallization.

Copper, gold and platinum group element geochemistry

The Niuatahi–Motutahi basalts contain 80–120 ppm Cu, 5·4–6·1 Au ppb, 6·72–8·25 ppb Pd, 1·18–4·73 ppb Pt, 0·03–0·32 ppb Rh, 0·027–0·089 ppb Ru, 0·016–0·055 ppb Ir and 0·28–0·32 ppb Re (Fig. 8; Table 2). The andesitic vesicle-filling glasses are more enriched in Cu, Au and Pd than the basalts, with 185–234 ppm of Cu, 4·7–6·9 ppb Au and 10–20 ppb of Pd. The uncertainty introduced by the correction was taken into account when propagating the uncertainty in the LA-ICP-MS Pd and Au values. Platinum and Ir-group platinum group element (IPGE) concentrations are positively correlated with MgO in the basalt, indicating that a Pt- and IPGE-rich phase crystallized along with the early formed olivine and clinopyroxene. On the other hand, Cu, Au and Pd increase with decreasing MgO and this trend continues into the andesitic vesicle-filling glasses (Fig. 8), indicating that these elements are behaving as incompatible elements during the early to middle stages of fractionation.

The Niuatahi–Motutahi dacites contain 80–201 ppm of Cu, <1–6·9 ppb of Au, 0·22–3·03 ppb of Pd, 0·05–0·52 ppb of Pt and <0·0006–0·033 ppb of Rh. Ruthenium and Ir concentrations of most samples are below the method detection limit of 1·2 ppt for Ru and 0·3 ppt for Ir, although some samples contain Ru and Ir concentrations of up to 0·032 ppb and 0·002 ppb, respectively (Tables 1 and 2). The Re contents of 0·51–0·70 ppb are significantly higher than those of the basalts. The abundances of Cu, Au, Pd, Pt and Rh decrease with decreasing MgO (Fig. 8), which shows that they behave compatibly during dacite differentiation. Rhenium abundance in the dacites ranges from 0·51 to 0·70 ppb and shows no clear correlation with increasing fractional crystallization. The Cu, Au and PGE data of the high-K and low-K dacites form a continuous trend, although the high-K dacites contain higher Cu, Au and

Downloaded from http://petrology.oxfordjournals.org/ by guest on January 20, 2015

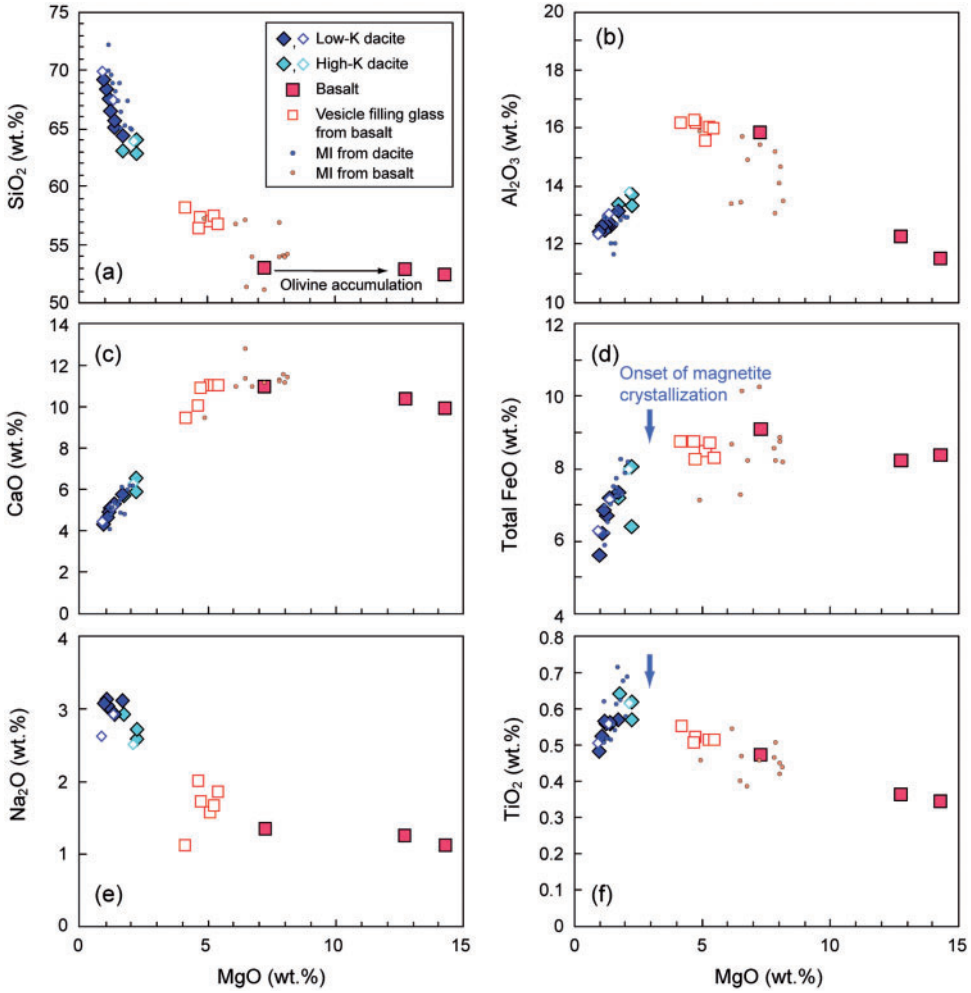

Fig. 5. (a–f) Major element variation diagrams for the Niuatahi–Motutahi lavas, melt inclusions and the glasses within them. MI, melt inclusion.

PGE contents than the low-K dacites because they have higher MgO.

The Niuatahi–Motutahi lavas show highly fractionated PGE patterns on a primitive mantle normalized diagram (Fig. 9) with Pd/Ir ratios of 140–516 for the basalts and >700 for the dacites. Dale *et al.* (2012), who analyzed the PGE concentrations of several Tonga arc lavas, including the Niuatahi–Motutahi lavas, also described similarly fractionated patterns (Fig. 9a). Patterns in the basalts rotate anticlockwise as MgO decreases, caused by the combined effects of the incompatible behavior of Pd, Au and Cu and compatible behavior of Pt, Rh, Ru and Ir during fractionation. In contrast, the patterns of the dacites are subparallel to each other and do not show any fractionation, although their abundances vary by more than an order of magnitude.

Description and composition of melt inclusions

Silicate melt inclusions occur in olivine and clinopyroxene phenocrysts in basalts and augite, pigeonite and plagioclase phenocrysts in dacites. The inclusions are mostly glassy, but some contain quench crystals. Fluid bubbles commonly occur within the glass inclusions. The size of the inclusions ranges from 10 to 100 μm. Some inclusions show evidence of post-entrapment crystallization along the inclusion walls and some olivine-hosted inclusions have Al-rich augite and magnetite as daughter minerals (Fig. 2d).

Melt inclusions without visible quench crystals were selected to correct for post-entrapment modification of the inclusions by crystallization of minerals along the inclusion walls. The correction was performed using the host mineral compositions, assuming equilibrium Mg–Fe partitioning between the host mineral and silicate melt (Putirka, 2008). Equilibrium olivine or pyroxene was incrementally added (0·1%) to the melt until its composition is in equilibrium with the host mineral. Before each addition Fe^{3+}/Fe^{2+} in the melt was calculated using the expression of Kress & Carmichael (1991) at 1200°C, 4 kbar, FMQ + 1 log units (where FMQ is fayalite–magnetite–quartz buffer) for inclusions from the basalts and 1000°C, 2 kbar, FMQ + 0·5 for inclusions from the dacites. The degree of post-entrapment crystallization obtained from the calculation was applied to correct the Cl and S concentrations, assuming both

Downloaded from http://petrology.oxfordjournals.org/ by guest on January 20, 2015

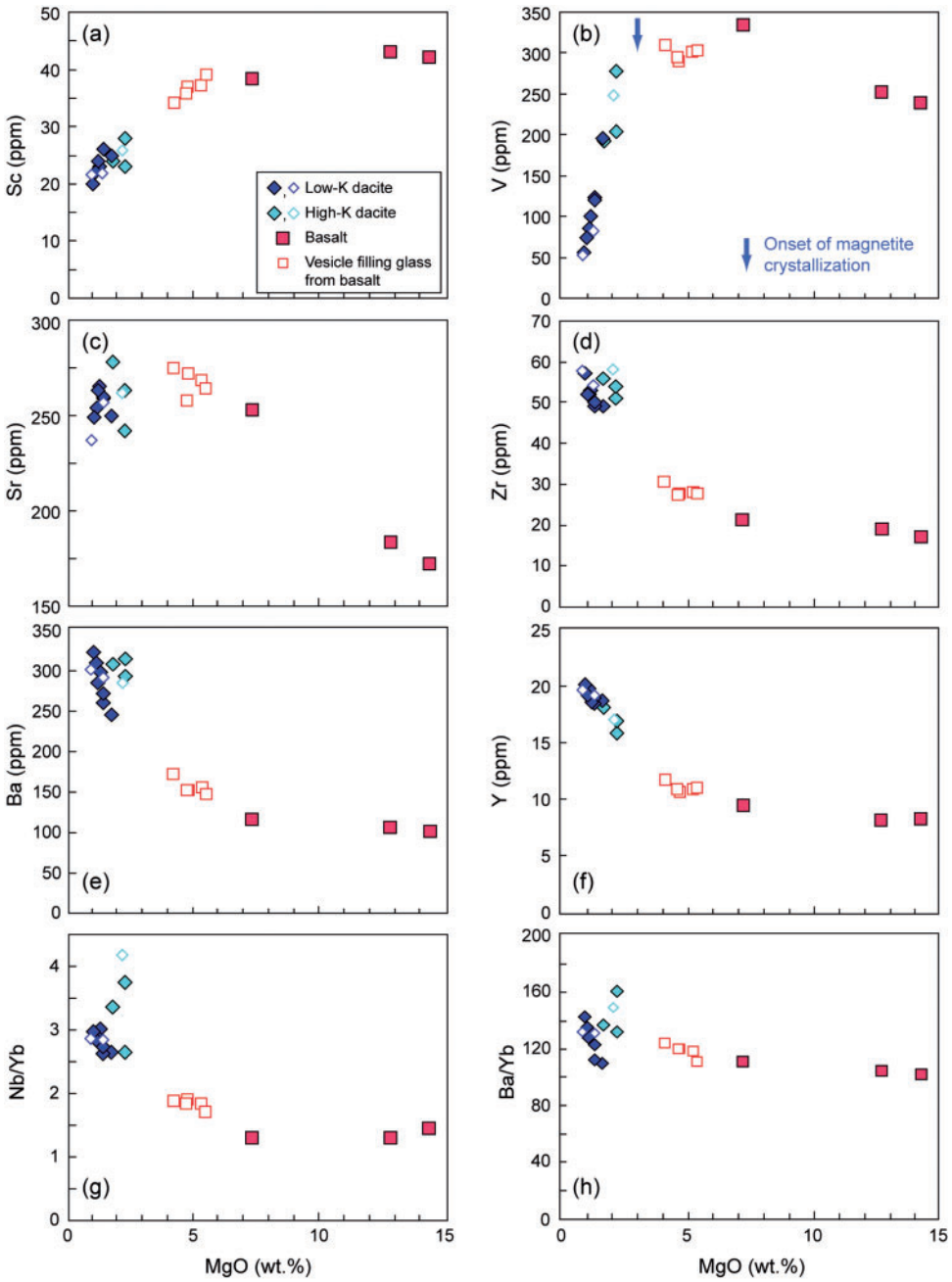

Fig. 6. (a–h) Selected trace element variation diagrams for the Niuatahi–Motutahi lavas.

elements are highly incompatible with a crystal–melt partition coefficient of 0·001.

The corrected melt inclusion compositions are illustrated in Fig. 5 (see Supplementary Data A for the melt inclusion compositions). The major element compositions of melt inclusions are generally consistent with the whole-rock or glass compositions, although Al_2O_3 concentrations of some melt inclusions extend to lower concentrations than those of the whole-rocks. It is also noteworthy that melt inclusions from the same sample are generally similar in composition (Fig. 5). This suggests that the phenocryst minerals that host the melt inclusions in a given rock are not xenocrysts. The melt inclusions from xenocrysts often have significantly different compositions compared with bulk-rocks and show wide compositional variations within a sample (e.g. Kamenetsky *et al.*, 2006). Danyushevsky *et al.* (2000) suggested that Fe loss can be caused by re-equilibration during cooling in olivine-hosted melt inclusions. Some olivine-hosted melt inclusions have lower FeO contents than their associated whole-rock, which is probably due to Fe loss during cooling. The low Al_2O_3 contents, relative to the bulk-rock compositions, may result from neglected Al-rich augite daughter crystals that could not be corrected for (Fig. 2d). The Na_2O contents of the melt inclusions are not

Downloaded from http://petrology.oxfordjournals.org/ by guest on January 20, 2015

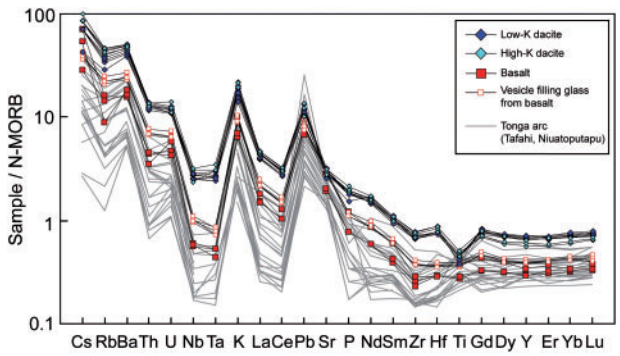

Fig. 7. Multi-element diagram normalized to the normal mid-ocean ridge basalt (N-MORB) values of Sun & McDonough (1989). The compositions of the Tafahi and Niuatoputapu Tonga arc volcanic rocks are taken from the GEOROC database (http://www.georoc.mpch-mainz.gwdg.de).

discussed in this paper because they may be affected by sodium loss during microprobe analysis (e.g. Morgan & London, 2005, and references therein). Because of their small size (<20 μm), most of the melt inclusions from the dacites were analyzed using a defocused 5 μm beam at 20 nA, which resulted in high current density leading to Na loss.

Temperature, pressure and oxygen fugacity

The liquidus temperatures and pressures of the Niuatahi–Motutahi melts were constrained by various thermobarometers (Supplementary Data A). Clinopyroxene and augite crystals and melt compositions were selected after applying the equilibrium test described by Putirka (2008). The clinopyroxene–melt thermometer (Putirka *et al.*, 2003) yielded temperatures of 1180–1220°C for the basalts and 880–1070°C for the dacites. These are similar to the temperature estimates from the clinopyroxene thermometer (1150–1200°C for the basalt; Nimis & Taylor, 2000) and liquid thermometer (960–1040°C for the dacite; Putirka, 2008). The high-K dacites have slightly higher temperatures than the low-K dacites, which is consistent with their higher MgO content. The pressure estimates, constrained by a clinopyroxene–melt barometer (Putirka, 2008), are in the range of 3·7–7·0 kbar (average = 5·5 ± 0·9, $n = 11$) for the basalt, 0·9–2·9 kbar (average = 1·9 ± 0·7, $n = 11$) for the low-K dacite, and 2·5–3·5 kbar for the high-K dacite (average = 2·8 ± 0·4, $n = 8$). Given that the Niuatahi–Motutahi lavas erupted at ~1700 m below sea level, ~0·2 kbar of the pressure can be attributed to seawater.

The olivine–spinel thermo-oxybarometer (Ballhaus *et al.*, 1991) was applied to olivine–Cr spinel pairs from the basalt. The temperature range obtained is 990–1110°C at 5·5 kbar, which is systematically ~100°C lower than the values estimated from the other thermometers. This may result from subsolidus re-equilibration between olivine and Cr spinel during cooling, or from a systematic bias in this method compared with other thermometers. The oxygen fugacity (fO_2), relative to the FMQ oxygen buffer, ranges from FMQ + 0·5 to FMQ + 2·9. The more mafic samples, DG26-1 and DG26-2, show lower fO_2 (average = FMQ + 1·0 ± 0·3, $n = 16$) compared with the less mafic sample, DG26-3 (average = FMQ + 2·5 ± 0·2, $n = 6$). The Cr spinels from DG26-3 are characterized by low Cr# (55–62) and their host olivines have low Mg# (80–83), showing that they have crystallized from a more evolved magma.

Bulk-rock Fe^{3+}/Fe^{2+}, measured by titration, was used to constrain the fO_2 of the dacites using the equation of Kress & Carmichael (1991). The estimated fO_2 at 1000°C and 2 kbar ranges from FMQ + 0·1 to 1·6. However, Sossi & O'Neill (2011) pointed out that the presence of reduced species such as S^{2-} in a silicate melt would lead to an underestimation of the bulk-rock Fe^{3+}/Fe^{2+} ratio because of the oxidation of S^{2-} to S^{6+} during titration. The sulfur contents in melt inclusions from the high-K dacite and low-K dacite are in the range of <190–207 ppm and 200–544 ppm, respectively. Assuming that 50% of S is dissolved as S^{2-} in a melt at an fO_2 of FMQ + 0·1 to +1·6 (Carroll & Rutherford, 1988), the corrected fO_2 values relative to the FMQ buffer are FMQ + 0·6 to +1·9 for the high-K dacites and FMQ + 0·4 to +0·5 for the low-K dacites (Table 1).

DISCUSSION

Magmatic differentiation of the Niuatahi–Motutahi magma

The Niuatahi–Motutahi lavas are temporally and spatially related to each other and occur within a limited area of ~15 km^2 around the Niuatahi–Motutahi volcano, which has been active until recently. Phenocrysts in the Niuatahi–Motutahi lavas are euhedral to subhedral and their compositions are in equilibrium with the bulk-rock composition, although some mafic basalt (>10 wt % MgO) samples contain accumulated early formed olivine. The phenocrysts are normally zoned with limited compositional variation and there is no mineralogical or petrological evidence for mixing or mingling between magma batches. Melt inclusions in phenocrysts have compositions consistent with those of the bulk-rocks. The major and trace element contents of the basalts, andesitic vesicle-filling glasses and dacites vary continuously, which can be explained by fractional crystallization of the observed phenocryst assemblages. MORB-normalized trace element patterns are subparallel to each other. Therefore, all the petrological and geochemical data suggest that the basalts and dacites are likely to be comagmatic and their compositional variations are dominated by fractional crystallization.

However, some dacites contain higher K_2O, LILE and Zr, Nb, Ta and Hf than the majority of the other dacites at the same MgO content (Figs 4–6). These high-K dacites (DG17-4, DG17-1, DG20-1) are characterized by higher Nb/Yb (2·7–3·7) and Ba/Yb (132–161) than the remainder of the Niuatahi–Motutahi dacites (Nb/Yb = 2·6–3·0; Ba/Yb = 110–143) (Fig. 6; Table 1). Nb/Yb

Downloaded from http://petrology.oxfordjournals.org/ by guest on January 20, 2015

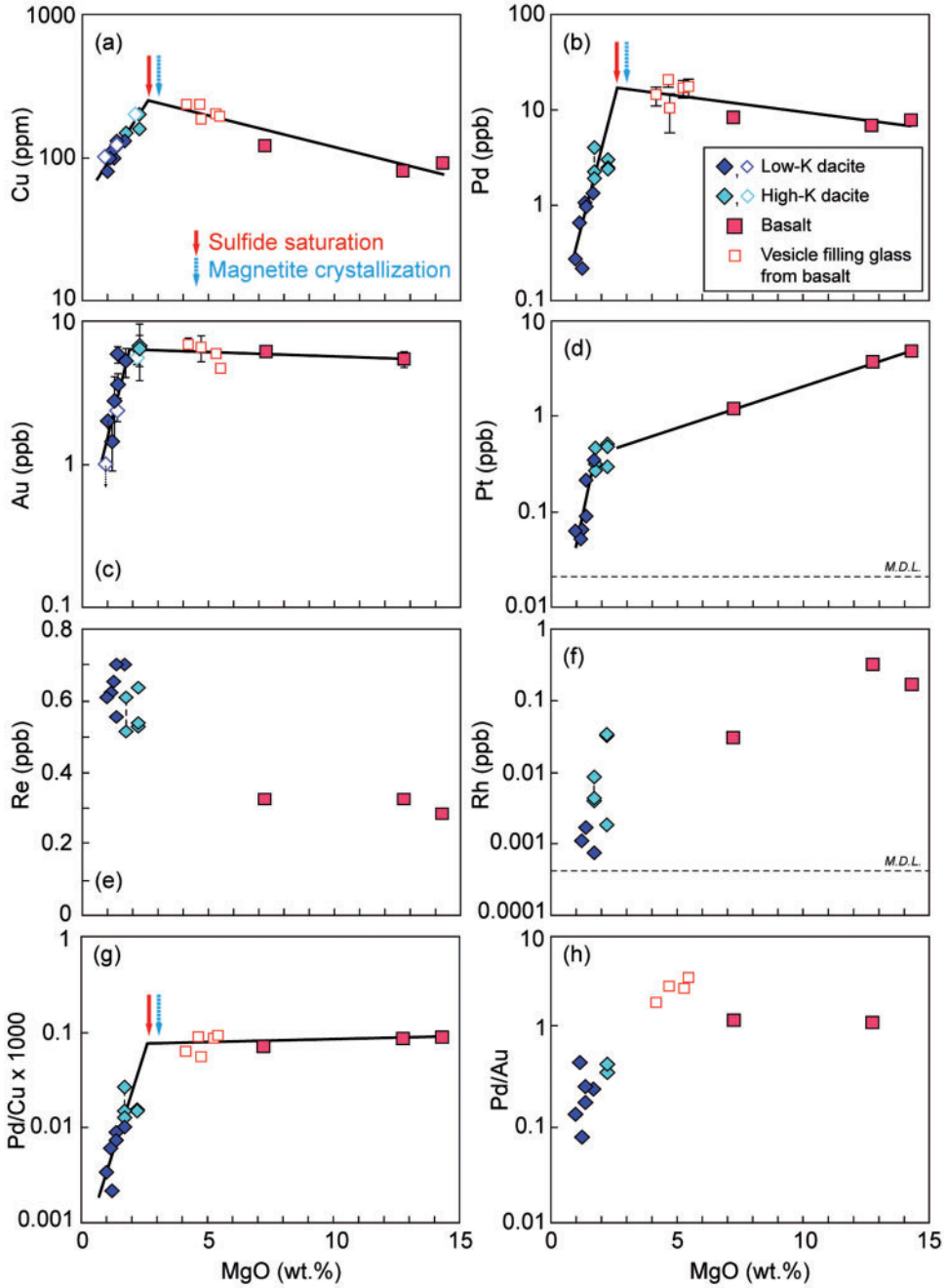

Fig. 8. (a–f) Variations in chalcophile element concentrations plotted versus MgO as a measure of fractionation for the Niuatahi–Motutahi lavas. Continuous lines are trend lines for basalts, vesicle-filling glasses, and low-K dacites. Solid and dotted arrows represent the timing of sulfide saturation and onset of magnetite crystallization, respectively. Vertical dotted lines link duplicate analyses. Horizontal dashed lines indicate method detection limits (MDL) for Pt and Rh. Data points with thin dotted arrows represents value below detection limits.

represents mantle fertility, and to some extent, degree of partial melting, whereas Ba/Yb is principally a measure of subduction input because Nb and Yb are immobile in subduction zones whereas Ba is subduction-mobile (Pearce & Stern, 2006). This suggests the high-K dacite primary magma may have been derived from a slightly more fertile source, or was produced by lower degree of partial melting with a larger subduction component than that of the low-K dacite. However, it should be noted that the Cu, Au and PGE contents of the high-K dacites are consistent with those of other dacites at the same degree of fractionation (Fig. 8), suggesting that chalcophile element contents in the parental magmas of both dacites were similar.

To investigate the genetic relationship between the basalts and two types of dacite we assessed the degree of fractional crystallization required to generate the dacites from the basalts using the least-squares mass-balance model of Cabero *et al.* (2012) and the observed crystal compositions (Table 3). About 50%

Downloaded from http://petrology.oxfordjournals.org/ by guest on January 20, 2015

Table 2: Platinum group element and Re concentrations (ppb) of the Niuatahi–Motutahi lavas

Sample	Re	Pd	Pt	Rh	Ru	Ir	Pd/Cu × 1000	Pd/Au
Basalt								
DG26-1	0·282	7·76	4·733	0·167	0·089	0·055	86	
DG26-2	0·324	6·72	3·678	0·318	0·078	0·041	84	1·2
DG26-3	0·325	8·25	1·183	0·030	0·027	0·016	69	1·4
*Andesitic vesicle-filling glass from basalt**								
DG26-2-VFG-2	n.d.	17·0 ± 3·5	n.d.	n.d.	n.d.	n.d.	77	2·9
DG26-2-VFG-3	n.d.	17·6 ± 3·8	n.d.	n.d.	n.d.	n.d.	83	3·7
DG26-2-VFG-4	n.d.	10·3 ± 4·5	n.d.	n.d.	n.d.	n.d.	67	
DG26-2-VFG-5	n.d.	14·1 ± 3·3	n.d.	n.d.	n.d.	n.d.	55	2·0
DG26-2-VFG-6	n.d.	20·4 ± 3·1	n.d.	n.d.	n.d.	n.d.	80	3·1
High-K dacite								
DG17-4	0·636	3·03	0·300	0·002	b.d.l.	b.d.l.	15·1	0·5
DG17-1 (#1)	0·526	2·47	0·520	0·032	0·002	0·002	15·4	0·4
DG17-1 (#2)	0·536	2·41	0·486	0·033	0·003	0·002	15·1	0·4
DG20-1 (#1)	0·608	2·26	0·315	0·004	b.d.l.	b.d.l.	15·1	
DG20-1 (#2)	0·515	4·01	0·469	0·009	0·002	0·002	26·7	
DG20-1 (#3)	0·513	1·92	0·270	0·004	b.d.l.	b.d.l.	12·8	
Low-K dacite								
DG18-1	0·701	1·33	0·354	0·001	b.d.l.	b.d.l.	10·2	0·3
DG24-1	0·556	1·07	0·090	b.d.l.	b.d.l.	b.d.l.	8·9	0·2
DG24-3	0·701	0·96	0·216	0·002	0·032	b.d.l.	7·4	0·3
DG23-1	0·653	0·22	0·064	0·001	b.d.l.	b.d.l.	2·2	0·1
DG16-4	0·622	0·66	0·051	b.d.l.	b.d.l.	b.d.l.	6·0	0·5
DG16-1	0·609	0·28	0·062	b.d.l.	b.d.l.	b.d.l.	3·4	0·1

n.d., not determined. b.d.l., below detection limit.
*Pd concentrations of the vesicle-filling glass are average of replicate analyses by LA-ICP-MS. The raw data are presented in Supplementary Data A. Large uncertainties (1σ) were derived from isobaric interference correction.

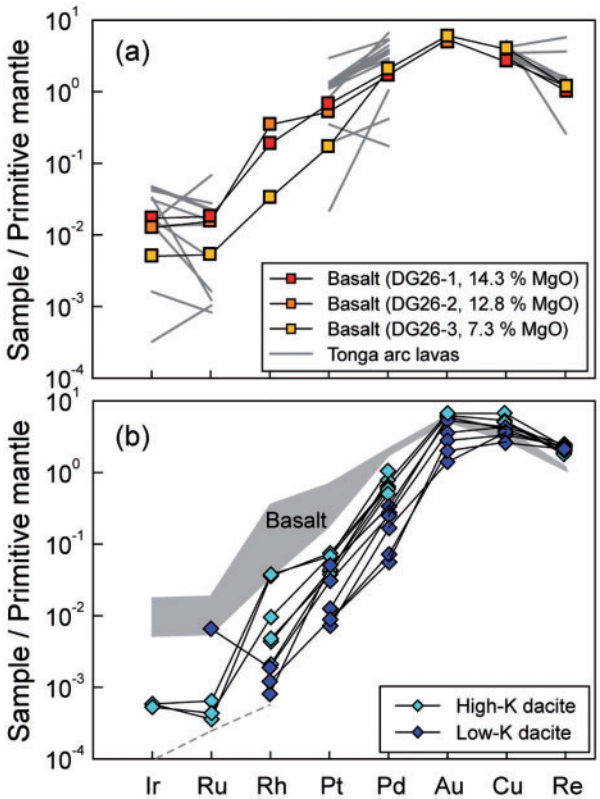

Fig. 9. (a, b) Primitive mantle-normalized PGE patterns for the Niuatahi–Motutahi lavas. The PGE data for Tonga arc lavas (Dale *et al.*, 2012) are shown for comparison. Dashed line represents method detection limits for Ir, Ru and Rh.

crystallization of the vesicle-filling glasses from basalts generated a good match for the composition of the least evolved low-K dacite, DG18-1; however, the model failed to produce the high-K dacite (DG 17-4). The sum of squared errors (SSE) of 0·21 is largely derived from Na_2O, which may be due to the Na loss during microprobe analysis of the vesicle-filling glass, as suggested above. If Na_2O is excluded from the model, the SSE decreases to <0·01. The REE contents of the low-K dacites were modeled using the mineral proportions from the least-squares model (Fig. 10). The REE abundances and patterns of the low-K dacites are also consistent with ~50% perfect fractional crystallization from the vesicle-filling glass from the basalt. The REE patterns of high-K dacites are characterized by enrichment of LREE and depletion of HREE relative to the low-K dacites and model estimates.

The Niuatahi–Motutahi basalt is considered to be representative of the parental magma of the low-K dacite, based on modeling constraints, and this conclusion is supported by their close temporal and spatial relationship, together with their mineralogy and geochemistry. A crystallization pressure of ~5 kbar obtained from clinopyroxene geobarometry indicates that the basaltic magma initially evolved in a magma chamber at a depth of ~15 km, the approximate depth of the crust–mantle boundary in this area (Contreras-Reyes *et al.*, 2011), and erupted directly through a NE–SW-trending fracture zone to form the volcanic complex SE of the caldera (Fig. 1). The augite from the low-K dacite crystallized at a pressure of 1·9 ± 0·7 kbar, suggesting that some of the evolved basaltic magma ascended to a high-level magma chamber at ~3–7 km depth and

Downloaded from http://petrology.oxfordjournals.org/ by guest on January 20, 2015

Table 3: Least-squares fractional crystallization modeling of the Niuatahi–Motutahi lavas

Melt composition	Parent (DG26-2-vesicle-filling glass)*	Daughter (DG18-1)	Calculation	Difference	SSE	R^2	F/C%
SiO_2	56·1	65·7	65·7	<0·01	0·21	1·00	–52·4
TiO_2	0·47	0·58	0·66	–0·07			
Al_2O_3	15·6	13·4	13·4	<0·01			
Fe_2O_3	9·33	8·33	8·33	<0·01			
MnO	0·20	0·14	0·18	–0·04			
MgO	5·21	1·72	1·71	<0·01			
CaO	10·8	5·85	5·84	<0·01			
Na_2O	1·66	3·18	2·86	0·32			
K_2O	0·66	1·04	1·36	–0·32			
Crystal composition	**Augite†**	**Clinopyroxene‡**	**Magnetite†**	**Pigeonite†**	**Plagioclase‡**		
SiO_2	51·7	53·1	0·13	52·1	46·5		
TiO_2	0·32	0·27	8·66	0·18			
Al_2O_3	1·57	2·36	2·75	0·84	34·9		
Fe_2O_3	16·5	7·78	91·3	28·6	0·82		
MnO	0·49	0·19	0·33	0·73			
MgO	13·7	17·2	1·60	20·3			
CaO	18·0	20·6	0·02	1·89	18·0		
Na_2O	0·13	0·14		0·02	1·11		
K_2O					0·04		
% crystallized	–5·3	–12·0	–1·2	–8·5	–25·4		
Recalculation at 100%	10·1	22·9	2·3	16·2	48·5		

*Average composition of the vesicle-filling glasses (>5 wt % MgO), normalized to 100%.
†Average compositions of augite, magnetite and pigeonite from the low-K dacites.
‡Average compositions of clinopyroxene and plagioclase from DG26-3.
SSE, sum of squared errors; F/C%, amount of crystallization from the parent melt.

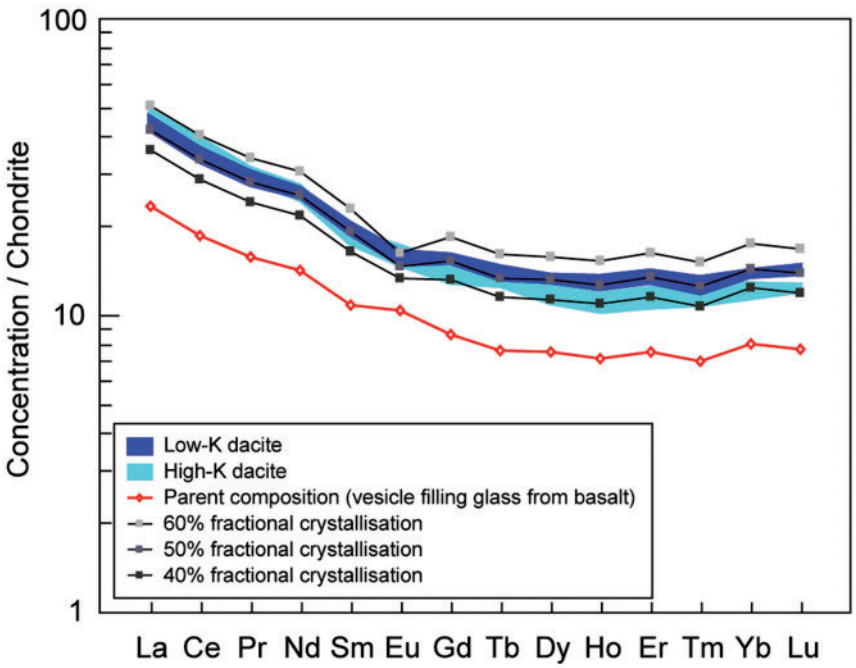

Fig. 10. Calculated REE patterns for the Niuatahi–Motutahi lavas with varying degrees of fractional crystallization from a basaltic andesitic parent, taken from the average composition of the vesicle-filling glasses. The chondrite normalizing values are from McDonough & Sun (1995). Mineral proportions used in the calculations are from Table 3. Mineral–melt partition coefficients are from McKenzie & O'Nions (1991), except for magnetite (Lemarchand *et al.*, 1987).

produced the low-K dacite by fractional crystallization. The high-K dacite may have been derived from a slightly different parental magma, which was produced by a lower degree of melting or melting of an enriched source with a larger subduction component.

Platinum-rich alloy saturation in the Niuatahi–Motutahi magma

The occurrence of Pt-rich alloys in arc-related settings suggests that Pt-rich alloy saturation may be a common feature of oxidized, subduction-related magmas. Park

Downloaded from http://petrology.oxfordjournals.org/ by guest on January 20, 2015

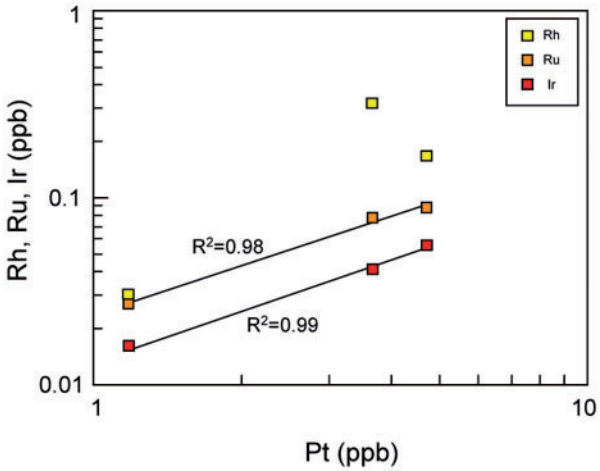

Fig. 11. Rhodium, Ru and Ir vs Pt diagram for the basalts.

et al. (2013*a*) investigated variations in PGE contents of andesitic–basaltic lavas of the Pual Ridge, Eastern Manus Basin, and showed that Pt behaved compatibly whereas Pd behaved incompatibly prior to sulfide saturation. They also compared PGE concentrations between phenocryst-bearing- and glassy samples, finding that the former are enriched in Pt and IPGE, but not Pd. They attributed these trends to the crystallization of a Pt-rich alloy along with the other silicate minerals during magma differentiation. Magmatic Pt-rich alloy inclusions were also observed in Cr spinels from the Ambae lavas, Vanuatu (Park *et al.*, 2012*a*) and volcanic ankaramite, Urals, Russia (Pushkarev *et al.*, 2014), indicating co-crystallization of Pt-rich alloy and Cr spinel. This is consistent with the presence of abundant Pt-rich alloys in arc cumulate rocks from the Greenhills complex, New Zealand (Spandler *et al.*, 2000, 2003), and the Uralian–Alaskan type Kytlym and Uktus complex, Russia (Garuti *et al.*, 2002).

The Pt contents of the Niuatahi–Motutahi basalts correlate positively with MgO (Fig. 8), and Pt and other PGE show positive correlations with each other except for Pd (Fig. 11 and Table 2). These trends are similar to those of the Pual Ridge lavas (Park *et al.*, 2013*a*), which were affected by Pt-alloy saturation. As mentioned above, the high-MgO basalts (>12 wt % MgO) resulted from the accumulation of early formed phenocrysts. Therefore, the high PGE contents of the high MgO samples, with the exception of Pd, are likely to be caused by the presence of Pt- and IPGE-rich phases trapped in phenocrysts. Cr-spinel fractionation may account for some of the Rh, Ru and Ir decrease as the Niuatahi–Motutahi lavas are oxidized (e.g. Park *et al.*, 2012*a*); however, Pt is not compatible in Cr spinel. Therefore, we suggest that Pt variation in the basalt can be explained only if the magma is saturated with a Pt-rich alloy.

The Pt-rich alloy saturation in subduction-related magmas is probably due to their low temperature, high Pt contents and delayed sulfide saturation. The liquidus temperature of arc basalts ranges from ~1100 to ~1200°C, which is ~100 to ~200°C lower than those of primitive ocean island basalts and komatiites. The Pt solubility is highly dependent on temperature and decreases with decreasing temperature (Fortenfant *et al.*, 2003). Under the conditions of formation of arc basalts, it falls to ~2 to ~10 ppb (e.g. Park *et al.*, 2013*a*) and this range overlaps with the reported Pt contents of basalts and picrites (Woodland *et al.*, 2002; Da *et al.*, 2012; Park *et al.*, 2012*a*, 2013*a*; this study). Mungall & Brenan (2014) suggested that the S content of a melt might increase its Pt solubility. However, this is unlikely to be an important consideration for the oxidized melts from which the Niuatahi–Motutahi Pt-rich alloys precipitated, because sulfate is expected to have been the dominant S species in the melt, and the presence of sulfate should not affect Pt solubility.

Dale *et al.* (2012) reported mildly compatible behavior for Pt in Volcano A, Tonga arc, but in this case it is unlikely to be due to Pt-rich alloy crystallization because the other PGE, including Pd, also behave compatibly in the suite. Given the mildly compatible behavior of all the PGE but the incompatible behavior of Cu in volcanic rocks from Volcano A, the magma may have undergone limited or localized sulfide segregation, resulting in a bulk D of >1 for the PGE, but bulk D < 1 for Cu.

Sulfide saturation history of the Niuatahi–Motutahi magma

Recent studies on the PGE geochemistry of intermediate to felsic rocks (Park *et al.*, 2013*a*, 2013*b*) show that sulfide saturation can be identified from variations in PGE, along with Cu and Au, in evolving magmatic systems. The Cu, Au and Pd contents progressively increase in the basalts and andesitic vesicle-filling glasses but abruptly decrease in the dacites (Fig. 8). The order of the rate of depletion is Pd > Au > Cu which is in order of decreasing partition coefficient and leads to a decrease in Pd/Cu and Pd/Au with decreasing MgO following sulfide saturation in the dacites (Fig. 8g and h). This suggests that the Niuatahi–Motutahi magma became sulfide saturated when it entered the dacitic phase of its evolution. This hypothesis is consistent with the presence of a Cu-rich sulfide bleb in the glass matrix of dacite sample DG24-3, which contains ~460 ppb of Pd and 1·2 ppm of Au (Fig. 2c; Supplementary Data B). We suggest that sulfide saturation occurred just before the magma evolved to a dacitic composition because the dacites still contain high abundances of chalcophile elements. Pd/Au ratios in the andesitic vesicle-filling glasses are slightly higher than those of basalts. This may be attributed to preferential Au loss by degassing during the formation of the vesicle-filling glasses, which are characterized by abundant bubbles (Fig. 2f). In contrast to other chalcophile elements, Re contents are higher in the dacites than in the basalts, showing that Re continues to behave as an incompatible element following sulfide saturation. This is because $D_{Re}^{sulfide-melt}$ is negatively correlated with oxygen fugacity and becomes <1 at QFM + 0·5 (Fonseca *et al.*, 2007). Magnetite

Downloaded from http://petrology.oxfordjournals.org/ by guest on January 20, 2015

crystallized from the dacites and can host some Re ($D_{Re}^{magnetite-melt} \sim 20$; Righter *et al.*, 1998); however, the bulk D value for the dacites is <1 because the modal abundance of magnetite <5%. This conclusion is supported by the least-squares model (Table 3).

The MgO content at sulfide saturation can be estimated from the intersection of extrapolations of Pd trends in the low-K dacites, vesicle-filling glasses and basalts. The two trend lines intersect at ~2·7 wt % MgO, shortly after magnetite saturation (Fig. 8), at an estimated Pd concentration of ~17 ppb (Fig. 8). The extrapolation of the Cu and Pd/Cu variation trends also provides consistent results, with intercepts at 2·6 wt % MgO (250 ppm Cu), and at 2·7 wt % MgO, where Pd/Cu is $6{\cdot}6 \times 10^{-5}$. This timing of sulfide saturation for the Niuatahi–Motutahi lava is relatively late compared with other arc lavas, most of which show earlier sulfide saturation (e.g. Lee *et al.*, 2012). Late sulfide saturation resulted in the Cu and Au content of the Niuatahi–Motutahi magmas increasing from 80 to 200 ppm Cu and from 5 to 7 ppb Au prior to sulfide saturation and the formation of the first dacites. These values are significantly higher than those of the average arc dacite (~30 ppm Cu and ~1 ppb Au; Robb, 2005).

Given that Cu is incompatible in the major crystallizing minerals in the dacites (e.g. Park *et al.*, 2013*a*, 2013*b*), removal of a sulfide melt has a major influence on the Cu content of the silicate melt. The fraction of sulfide melt precipitating from the silicate melt required to explain the observed variation in Cu in the Niuatahi–Motutahi dacites is 0·2 wt %, assuming $D_{Cu}^{sulfide-melt} = 1300$ (Ripley *et al.*, 2002). This is consistent with the sulfide fraction of 0·2–0·3 wt % determined for other sulfide-saturated magmas (e.g. Jamais *et al.*, 2008; Park *et al.*, 2013*a*).

There is a limited number of experimental studies on sulfur solubility in silicate melts at temperatures below 1100°C. Carroll & Rutherford (1985, 1988) and Luhr (1990) investigated the sulfur solubility in a hydrous trachyandesite at ~950–1000°C and 2 kbar with fO_2 varying between FMQ and FMQ + 1, conditions similar to those of the Niuatahi–Motutahi magma. They showed ~300–550 ppm of S dissolved in a melt in equilibrium with FeS. The sulfur contents of melt inclusions in the low-K dacites range from <200 to 544 ppm, which is consistent with the experimental constraints. However, the sulfur concentrations of the melt inclusions in the high-K dacites only rarely exceed 200 ppm, suggesting that the melt inclusions may have been trapped after magma degassing.

The sulfur solubility in a silicate melt is a function of several parameters, including fO_2, temperature and the FeO content of the melt (Carroll & Rutherford, 1985; Luhr, 1990; O'Neill & Mavrogenes, 2002). The onset of magnetite crystallization decreases not only the Fe content of the melt but also Fe^{3+}/Fe^{2+}, which lowers fO_2 and sulfur solubility in the melt (e.g. Jenner *et al.*, 2010), converting highly soluble sulfate in the melt to less soluble sulfide. The total FeO, Ti and V contents decrease below 3 wt % MgO in the Niuatahi–Motutahi dacites, which suggests that the onset of magnetite crystallization at ~3 wt % MgO (Fig. 5) was the trigger for sulfide saturation. Furthermore, magnetite is a common phenocryst mineral in these rocks. This is also consistent with the difference in the estimated fO_2 between the basalts and the dacites. The fO_2 increased in the basalt from FMQ + 1 to FMQ + 2·5 during the early stages of magma differentiation, which are dominated by olivine fractionation. However, following magnetite saturation this falls to ~ FMQ + 0·5 in the dacite (Table 1 and Supplementary Data A).

Volatile saturation history of the Niuatahi–Motutahi lava

The Niuatahi–Motutahi basalts and dacites have varying amounts of vesicles. This indicates magma degassing during ascent prior to eruption. A CO_2-rich vapour phase predominates in basaltic magmas at high pressure, but H_2O becomes the dominant component in more evolved magmas at low pressure (Dixon & Stolper, 1995; Newman & Lowenstern, 2002; Lesne *et al.*, 2011; Baker & Alletti, 2012). Sulfur and Cl behave incompatibly during magma evolution at high pressure, but start to degas at shallow depths of <~2 kbar (Lesne *et al.*, 2011).

Native sulfur mineralization occurs in association with the dacites, which suggests that a S-rich magmatic gas exsolved from the dacitic magma. Volatile element analyses provide information on the composition of the magmatic gas and the timing of volatile saturation. Chlorine contents in melt inclusions and vesicle-filling glass from the basalts range from 987 to 1596 ppm, which is about half of the Cl contents in melt inclusions and glasses (2210–3850 ppm) in the dacites (Supplementary Data A). The Cl concentrations broadly increase with decreasing MgO in the basalts, andesitic vesicle-filling glasses and dacites (Fig. 12). Sulfur concentrations in the melt inclusions from the basalts range from <150 to 513 ppm. The melt inclusions from the dacites contain a similar range of S contents from <190 to 544 ppm, although most of the melt inclusions from the high-K dacites contain less than 190 ppm S. It should also be noted that the S contents of the vesicle-filling glasses in the dacites and the dacitic glasses themselves are below the detection limit of ~200 ppm, which is consistently lower than those of melt inclusions owing to S loss during eruption.

Fractional crystallization modeling of Cl and S contents in a melt was carried out using the average composition of the melt inclusion, and assumed mineral–melt partition coefficients for Cl and S of 0·001. The bulk partition coefficient for Mg of 3·24 was calculated from the mineral proportions and its composition from the least-squares model of Cabero *et al.* (2012) (Table 3). As suggested by the Pd and Cu data, 0·2% of sulfide melt removal was added to the model for MgO

Downloaded from http://petrology.oxfordjournals.org/ by guest on January 20, 2015

values below 2·7 wt % (Model 1 in Fig. 12). Model 1 explains the variation of Cl, but the S contents of the dacites are substantially lower than the estimated values. This requires additional S loss by degassing of the S-rich magma. During magmatic gas exsolution both Cl and S partition into the gas phase; however, S generally starts to degas earlier than Cl during magma ascent and evolution (Lesne *et al.*, 2011) and the partition coefficient between the magmatic vapor and melt is much higher for S than Cl (Botcharnikov *et al.*, 2004). Model 2 added 5% of gas exsolution to Model 1 using $D_{Cl}^{vapor-melt} = 10$ (Webster *et al.*, 2009) and $D_{S}^{vapor-melt} = 50$ (Webster & Botcharnikov, 2011), with exsolution starting at 2 wt % MgO. Model 2 is generally consistent with the trends for S and Cl contents in the melt inclusions from the dacites. This suggests that S- and Cl-bearing gas exsolution may have occurred during dacitic magma evolution. Copper and Au partition into the volatile phase together with S and Cl (Hedenquist & Lowenstern, 1994; Williams-Jones & Heinrich, 2005; Mavrogenes *et al.*, 2010) so that when the magmatic vapor ascended to the ocean floor it condensed to form the observed Cu- and Au-rich native sulfur mineralization (Kim *et al.*, 2011).

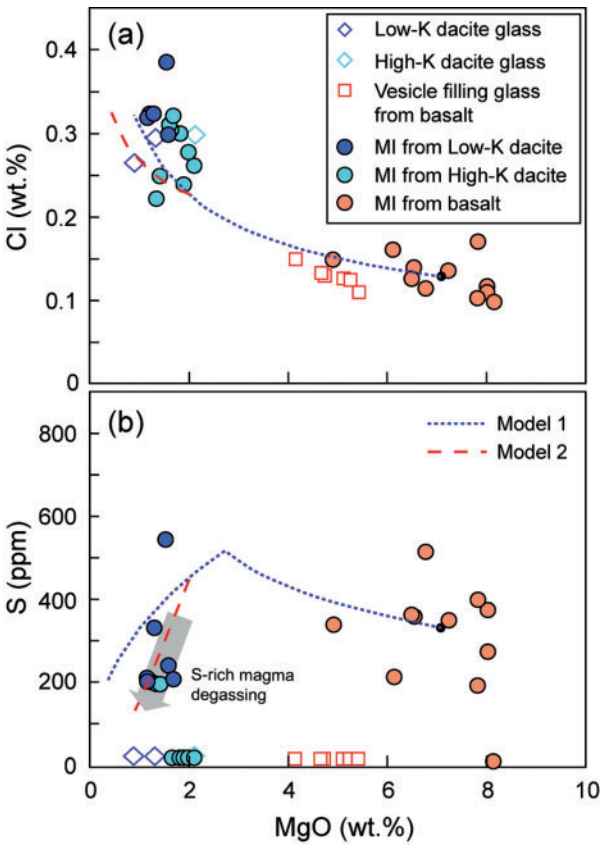

Fig. 12. (a, b) Chlorine and S variation diagrams for melt inclusions (MI), glass and vesicle-filling glass from the Niuatahi–Motutahi lavas. Model 1 represents the fractional crystallization trend for silicate and oxide minerals with removal of sulfide melt at 2·7 wt % MgO, assuming a sulfide fraction of 0·2 wt %. Model 2 includes 5 wt % gas exsolution at 2 wt % MgO. The average composition of melt inclusions from the basalts was used as the parent magma. For plotting purposes, S values below the detection limit are plotted as zero.

The role of sulfide saturation in the formation of Cu- and Au-rich magmas

Most magmatic–hydrothermal Cu and/or Au deposits, such as porphyry deposits, are genetically linked to arc magmas (Seedorff *et al.*, 2005; Sillitoe, 2010). However, the majority of arc magmas are barren and not associated with economic mineralization. This has led to studies aimed at identifying the distinctive characteristics of ore-bearing arc magmas compared with barren systems. It has been suggested that certain types of arc-associated magmas have a close relationship with large Cu and/or Au deposits. Among these are adakitic magmas, as described by Mungall (2002) and Sun *et al.* (2011), and alkaline magmas, as described by McInnes *et al.* (1999). These workers emphasized the importance of magma sources and melting conditions in the formation of Cu and/or Au deposits. They suggested that these types of arc magmas contain higher initial abundances of chalcophile elements than normal arc magmas, which makes them fertile sources for mineralization.

However, the chalcophile element geochemistry of the Niuatahi–Motutahi lavas shows that the timing of sulfide saturation may also play an important role in the formation of fertile (i.e. Cu- and Au-rich) magmas as was previously suggested by several researchers (Candela & Holland, 1986; Keith *et al.*; 1997; Jenner *et al.*, 2010; Richards, 2011; Wilkinson, 2013). Figure 13 shows the Cu data for the Niuatahi–Motutahi lavas and compares these with those for volcanic rocks from the Honshu arc. The Cu concentrations of the majority of

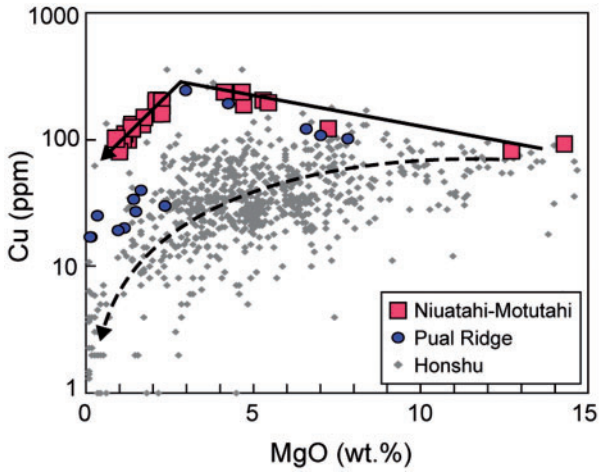

Fig. 13. Comparison of Cu variations in the Niuatahi–Motutahi lavas, Pual Ridge lavas from the eastern Manus Basin and Honshu arc volcanic rocks. Continuous-line and dashed-line arrows represent the inferred magma differentiation paths of the Niuatahi–Motutahi lavas and Honshu arc volcanic rocks, respectively. The MgO and Cu data for the Pual Ridge lavas are from Sun *et al.* (2007) and those for the Honshu volcanic rocks are from the GEOROC database (http://www.georoc.mpch-mainz, gwdg.de).

Downloaded from http://petrology.oxfordjournals.org/ by guest on January 20, 2015

the Honshu volcanic rocks decrease with decreasing MgO, highlighting the influence of sulfide saturation on the magma differentiation trend, which is distinct from that defined by the Niuatahi–Motutahi lavas. Early sulfide saturation results in very low Cu contents (average 19 ppm) in the dacites of the Honshu arc. This suggests that the absence of porphyry Cu deposit in Japan is probably due to the low Cu contents of the evolved volcanic rocks, especially the dacitic porphyries, as suggested by Sato (2012) and Richards & Mumin (2013), because the potentially Cu deposit-forming volatiles originate from these Cu-poor magmas (Seedorff *et al.*, 2005).

It should be noted that the Cu contents of both the Niuatahi–Motutahi lavas and Honshu volcanic rocks with MgO contents higher than 10 wt % are comparable, which suggests that the initial Cu contents of the primary magmas were similar. What produced the two different Cu trends in the magma differentiation processes? The basement of the Japanese islands, which was intruded by Cretaceous to Paleogene Honshu arc magmas, consists mainly of a Paleozoic accretionary complex containing carbonaceous sedimentary rocks (Sato, 2012, and references therein). Therefore, the Honshu magmas were likely to assimilate lower crustal, carbon-rich, sedimentary materials, which may have lowered the fO_2 of the melt, leading to early sulfide saturation (Sato, 2012; Richards & Mumin, 2013). This suggestion is consistent with the result of a recent study by Tomkins *et al.* (2012) on the petrogenesis of the Opirarukaomappu Gabbroic Complex (OGC), Japan, which is associated with massive–disseminated sulfide Ni–Cu mineralization. They suggested that mixing between a S- and Cu-rich mantle-derived basaltic magma and a C-rich crust-derived tonalitic magma caused the sulfide mineralization. The intrusion of basalt into the carbonaceous lower crust induced crustal melting and produced carbon-rich, reduced felsic magmas. This process might be a common feature of arc magmas because the exposed island arc sequences often contain carbon-rich accretionary complexes (Tomkins *et al.*, 2012).

In contrast, the early stage of evolution of the Niuatahi–Motutahi magmas was dominated by fractional crystallization of Cu-poor minerals, which concentrated Cu in the melt. Sulfide saturation was delayed until a late stage in magma evolution. This allowed the Niuatahi–Motutahi magmas to become enriched in chalcophile elements until S-rich volatile exsolution occurred at ~2 wt % MgO. It should be noted that the Cu and Au contents of the Niuatahi–Motutahi dacites were about an order of magnitude higher than those of the Honshu dacites (19 ppm Cu and 0·2 ppb Au; Togashi & Terashima, 1997) at the time of volatile exsolution. We suggest that this magmatic vapor produced the Niuatahi–Motutahi Cu–Au-rich native sulfur mineralization. The highly oxidized nature of the Niuatahi–Motutahi basalt (QFM + 1 to +2·5) may have been a critical factor in delaying sulfide saturation because within this fO_2 range sulfur solubility in the melt is strongly fO_2 dependent (Carroll & Rutherford, 1988; Jugo, 2009). In addition, the Niuatahi–Motutahi magma ascended through the Tonga arc crust, which is thin (~15–20 km) and composed of basaltic rocks (Contreras-Reyes *et al.*, 2011). Therefore, crustal assimilation would have been minimal and any crust that was assimilated would have been C-poor. The Pual Ridge lavas of the Eastern Manus Basin, which are associated with seafloor Cu–Au mineralization, are also characterized by incompatible behavior of Cu and Au during early magma differentiation (Park *et al.*, 2013*a*), which suggests that late sulfide saturation resulted in the Pual Ridge magma being enriched in Cu and Au by the time of water-rich volatile exsolution.

It has been suggested that sulfide blebs can act as a reservoir of ore metals and S (e.g. Keith *et al.*, 1997; Halter *et al.*, 2002; Nadeau *et al.*, 2010). Halter *et al.* (2002) investigated Cu, Au and Fe contents in silicate and sulfide melt inclusions in amphibole phenocrysts from volcanic and intrusive rocks from the Farallon Negro Volcanic Complex in northwestern Argentina that hosts the large Bajo de la Alumbrera porphyry Cu–Au deposit. Based on Cu and Au concentrations, and the similar Au/Cu ratio of sulfide melt inclusions and fluid inclusions of an early hydrothermal brine, they suggested that the magma associated with the deposit was sulfide saturated but that the early formed sulfide blebs were destabilized during volatile exsolution and the Cu, Au and S in the sulfide blebs migrated into the ore-forming fluid. Nadeau *et al.* (2010) studied sulfide and silicate melt inclusions that occur in the volcanic rocks from the Merapi Volcano, Indonesia. They reported numerous partially or almost completely dissolved sulfide inclusions associated with silicate melt inclusions and fluid inclusions, and argued that these textures suggest interaction between the sulfide blebs and a hydrothermal fluid. Based on this evidence, and similar metal ratios in sulfide melt inclusions and volcanic gas collected from the volcano, they proposed that sulfide blebs in a mafic magma were injected into a more evolved felsic magma where they dissolved and that the metals in the sulfide blebs were transferred to a volcanic gas phase during decompression of the mafic magma.

Volatile exsolution and sulfide segregation occur at the same time in the Niuatahi–Motutahi dacites so it is likely that there was some interaction between sulfide blebs and the exsolved magmatic vapor in the magma chamber; however, the decrease of PGE in the dacites rules out complete dissolution of the sulfide blebs. Furthermore, dissolution of the sulfide blebs would have been limited to those held in suspension in the convecting magma and blebs near the crystal–liquid interface of the solidifying magma chamber. We therefore suggest that localized or limited dissolution of sulfide blebs may have additionally enriched the magmatic gas in Cu and Au at Niuatahi–Motutahi.

Downloaded from http://petrology.oxfordjournals.org/ by guest on January 20, 2015

This study shows that the timing of sulfide saturation is a critical factor to form a magma enriched in chalcophile elements. Once a mantle-derived basaltic magma rises into the crust, the fO_2, temperature and FeO content of the magma control sulfur solubility in the silicate melt. Assimilation of reducing crustal materials and mixing with a crust-derived silicic magma are the processes most likely to result in sulfide saturation during open-system magma differentiation, whereas reduction produced by magnetite crystallization is likely to be the dominant process in closed systems. A magma that reaches sulfide saturation early and precipitates a significant amount of sulfide melt before it becomes volatile saturated is unlikely to produce a magmatic–hydrothermal ore deposit because ore metals, such as Cu and Au, will be held in the crystallizing magma chamber, leading to a residual magma that is depleted in these elements.

CONCLUSIONS

The Niuatahi–Motutahi lavas are temporally and spatially associated basaltic and dacitic submarine volcanic rocks. They show geochemical features that are typical of island arc magmas, with enrichment of LILE relative to MORB and pronounced negative Nb and Ta anomalies. Two types of dacites occur within the Niuatahi–Motutahi region: the high-K dacite and low-K dacite. Modeling shows that the low-K dacites can be produced by ~50% fractional crystallization of the magma, as represented by andesitic glass found as a vesicle filling in the basalts, indicating a comagmatic origin for the low-K dacites and basalts. The high-K dacites may have originated from a slightly different parent magma that is more fertile and more enriched in subduction components relative to that of the low-K dacites. The PGE geochemistry of the Niuatahi–Motutahi lavas suggests Pt-rich alloy crystallization during fractionation of the basalts and andesites and sulfide saturation in the dacite. The timing of sulfide saturation was late, which allowed the Niuatahi–Motutahi dacite to concentrate Cu and Au prior to volatile saturation, and form the Cu- and Au-rich native sulfur mineralization in this region, despite unremarkable chalcophile element concentrations in the parental magma. In contrast, the Honshu arc magmas are characterized by early sulfide saturation and the Honshu dacites are impoverished in Cu, and probably Au and Pd, which accounts for the absence of Cu porphyries in Japan. This study shows that the timing of sulfide saturation and the amount of sulfide precipitation during magma differentiation play important roles in the formation of fertile (Cu- and Au-rich) magmas.

ACKNOWLEDGEMENTS

We are grateful to Jeremy Richards, Vadim Kamenetsky and Christopher Dale for their constructive and helpful reviews, and to Richard Price for thoughtful comments as an editor. We thank Robert Rapp for his help during electron microprobe analysis, Richard Henley for his valuable comments on volatile exsolution processes, and Paolo Sossi for his comments on the effect of dissolved S on titration data and for proofreading.

FUNDING

This research was supported by an Australian Research Council Discovery grant to Ian Campbell and a fund from the Ministry of Oceans and Fisheries of Korea (PM57580). Three-month stipend for Jung-Woo Park was supported by Australian Research Council grant to Oliver Nebel in 2012.

SUPPLEMENTARY DATA

Supplementary data for this paper are available at *Journal of Petrology* online.

REFERENCES

Arculus, R. J. (2005). Arc–backarc systems of northern Kermadec–Tonga. In: *Realising New Zealand's Mineral Potential - Proceedings of 2005 New Zealand Minerals Conference*. New Zealand Ministry of Economic Development, pp. 45–50.

Baker, D. R. & Alletti, M. (2012). Fluid saturation and volatile partitioning between melts and hydrous fluids in crustal magmatic systems: The contribution of experimental measurements and solubility models. *Earth-Science Reviews* **114**, 298–324.

Ballhaus, C., Berry, R. F. & Green, D. H. (1991). High-pressure experimental calibration of the olivine–orthopyroxene–spinel oxygen geobarometer—implications for the oxidation-state of the upper mantle. *Contributions to Mineralogy and Petrology* **107**, 27–40.

Botcharnikov, R. E., Behrens, H., Holtz, F., Koepke, J. & Sato, H. (2004). Sulfur and chlorine solubility in Mt. Unzen rhyodacitic melt at 850°C and 200 MPa. *Chemical Geology* **213**, 207–225.

Cabero, M. T., Mecoleta, S. & Lopez-Moro, F. J. (2012). OPTIMASBA: A Microsoft Excel workbook to optimise the mass-balance modelling applied to magmatic differentiation processes and subsolidus overprints. *Computers and Geosciences* **42**, 206–211.

Candela, P. A. (1997). A review of shallow, ore-related granites: Textures, volatiles, and ore metals. *Journal of Petrology* **38**, 1619–1633.

Candela, P. A. & Holland, H. D. (1986). A mass-transfer model for copper and molybdenum in magmatic hydrothermal systems—the origin of porphyry-type ore-deposits. *Economic Geology* **81**, 1–19.

Carroll, M. R. & Rutherford, M. J. (1985). Sulfide and sulfate saturation in hydrous silicate melts. *Journal of Geophysical Research* **90**, C601–C612.

Carroll, M. R. & Rutherford, M. J. (1988). Sulfur speciation in hydrous experimental glasses of varying oxidation-state—results from measured wavelength shifts of sulfur X-rays. *American Mineralogist* **73**, 845–849.

Contreras-Reyes, E., Grevemeyer, I., Watts, A. B., Flueh, E. R., Peirce, C., Moeller, S. & Papenberg, C. (2011). Deep seismic structure of the Tonga subduction zone: Implications for mantle hydration, tectonic erosion, and arc magmatism.

Downloaded from http://petrology.oxfordjournals.org/ by guest on January 20, 2015

Journal of Geophysical Research: Solid Earth **116**, doi:10.1029/2011JB008434.

Dale, C. W., Macpherson, C. G., Pearson, D. G., Hammond, S. J. & Arculus, R. J. (2012). Inter-element fractionation of highly siderophile elements in the Tonga Arc due to flux melting of a depleted source. *Geochimica et Cosmochimica Acta* **89**, 202–225.

Danyushevsky, L. V., Della-Pasqua, F. N. & Sokolov, S. (2000). Re-equilibration of melt inclusions trapped by magnesian olivine phenocrysts from subduction-related magmas: petrological implications. *Contributions to Mineralogy and Petrology* **138**, 68–83.

Dixon, J. E. & Stolper, E. M. (1995). An experimental study of water and carbon dioxide solubilities in mid-ocean ridge basaltic liquids. 2. Applications to degassing. *Journal of Petrology* **36**, 1633–1646.

Ebel, D. S. & Naldrett, A. J. (1997). Crystallization of sulfide liquids and the interpretation of ore composition. *Canadian Journal of Earth Sciences* **34**, 352–365.

Fonseca, R. O. C. (2007). The high-temperature geochemistry of the highly siderophile elements, Pt, Re, Ir, Os and Rh. Canberra: Australian National University.

Fonseca, R. O. C., Mallmann, G., O'Neill, H. S. C. & Campbell, I. H. (2007). How chalcophile is rhenium? An experimental study of the solubility of Re in sulphide mattes. *Earth and Planetary Science Letters* **260**, 537–548.

Fortenfant, S. S., Gunther, D., Dingwell, D. B. & Rubie, D. C. (2003). Temperature dependence of Pt and Rh solubilities in a haplobasaltic melt. *Geochimica Et Cosmochimica Acta* **67**, 123–131.

Garuti, G., Pushkarev, E. V. & Zaccarini, F. (2002). Composition and paragenesis of Pt alloys from chromitites of the Uralian–Alaskan-type Kytlym and Uktus complexes, northern and central Urals, Russia. *Canadian Mineralogist* **40**, 1127–1146.

Govindaraju, K. (2007). 1994 compilation of working values and sample description for 383 geostandards. *Geostandards Newsletter*, doi: 10.1046/j.1365-2494.1998.53202081.x-i1.

Halter, W. E., Pettke, T. & Heinrich, C. A. (2002). The origin of Cu/Au ratios in porphyry-type ore deposits. *Science* **296**, 1844–1846.

Hedenquist, J. W. & Lowenstern, J. B. (1994). The role of magmas in the formation of hydrothermal ore-deposits. *Nature* **370**, 519–527.

Jamais, M., Lassiter, J. C. & Brugmann, G. (2008). PGE and Os-isotopic variations in lavas from Kohala Volcano, Hawaii: Constraints on PGE behavior and melt/crust interaction. *Chemical Geology* **250**, 16–28.

Jenner, F. E., O'Neill, H. S. C., Arculus, R. J. & Mavrogenes, J. A. (2010). The magnetite crisis in the evolution of arc-related magmas and the initial concentration of Au, Ag and Cu. *Journal of Petrology* **51**, 2445–2464.

Jochum, K. P. & Nohl, U. (2008). Reference materials in geochemistry and environmental research and the GeoReM database. *Chemical Geology* **253**, 50–53.

Jochum, K. P., Weis, U., Stoll, B., Kuzmin, D., Yang, Q. C., Raczek, I., Jacob, D. E., Stracke, A., Birbaum, K., Frick, D. A., Gunther, D. & Enzweiler, J. (2011). Determination of reference values for NIST SRM 610–617 glasses following ISO guidelines. *Geostandards and Geoanalytical Research* **35**, 397–429.

Jugo, P. J. (2009). Sulfur content at sulfide saturation in oxidized magmas. *Geology* **37**, 415–418.

Kamenetsky, V. S., Elburg, M., Arculus, R. & Thomas, R. (2006). Magmatic origin of low-Ca olivine in subduction-related magmas: Co-existence of contrasting magmas. *Chemical Geology* **233**, 346–357.

Keith, J. D., Whitney, J. A., Hattori, K., Ballantyne, G. H., Christiansen, E. H., Barr, D. L., Cannan, T. M. & Hook, C. J. (1997). The role of magmatic sulfides and mafic alkaline magmas in the Bingham and Tintic mining districts, Utah. *Journal of Petrology* **38**, 1679–1690.

Keller, N. S., Arculus, R. J., Hermann, J. & Richards, S. (2008). Submarine back-arc lava with arc signature: Fonualei Spreading Center, northeast Lau Basin, Tonga. *Journal of Geophysical Research: Solid Earth* **113**, doi: 10.1029/2007JB005451.

Kim, J., Son, S. K., Son, J. W., Kim, K. H., Shim, W. J., Kim, C. H. & Lee, K. Y. (2009). Venting sites along the Fonualei and Northeast Lau Spreading Centers and evidence of hydrothermal activity at an off-axis caldera in the northeastern Lau Basin. *Geochemical Journal* **43**, 1–13.

Kim, J., Lee, K. Y. & Kim, J. H. (2011). Metal-bearing molten sulfur collected from a submarine volcano: Implications for vapor transport of metals in seafloor hydrothermal systems. *Geology* **39**, 351–354.

Kress, V. C. & Carmichael, I. S. E. (1991). The compressibility of silicate liquids containing Fe_2O_3 and the effect of composition, temperature, oxygen fugacity and pressure on their redox states. *Contributions to Mineralogy and Petrology* **108**, 82–92.

Kullerud, G., Yund, R. A. & Moh, G. (1966). Phase relations in Fe–Ni–S, Cu–Fe–S and Cu–Ni–S systems. *Economic Geology* **61**, 323–343.

Lee, C. T. A., Luffi, P., Chin, E. J., Bouchet, R., Dasgupta, R., Morton, D. M., Le Roux, V., Yin, Q. Z. & Jin, D. (2012). Copper systematics in arc magmas and implications for crust–mantle differentiation. *Science* **336**, 64–68.

Le Maitre, R. W. (1984). A proposal by the IUGS Subcommission on the Systematics of Igneous Rocks for a chemical classification of volcanic rocks based on the total alkali–silica (TAS) diagram. *Australian Journal of Earth Sciences* **31**, 243–255.

Lemarchand, F., Villemant, B. & Calas, G. (1987). Trace-element distribution coefficients in alkaline series. *Geochimica et Cosmochimica Acta* **51**, 1071–1081.

Lesne, P., Kohn, S. C., Blundy, J., Witham, F., Botcharnikov, R. E. & Behrens, H. (2011). Experimental simulation of closed-system degassing in the system basalt–H_2O–CO_2–S–Cl. *Journal of Petrology* **52**, 1737–1762.

Longerich, H. P., Jackson, S. E. & Gunther, D. (1996). Laser ablation inductively coupled plasma mass spectrometric transient signal data acquisition and analyte concentration calculation. *Journal of Analytical Atomic Spectrometry* **11**, 899–904.

Luhr, J. F. (1990). Experimental phase relations of water-saturated and sulfur-saturated arc magmas and the 1982 eruptions of El Chichon Volcano. *Journal of Petrology* **31**, 1071–1114.

Mavrogenes, J., Henley, R. W., Reyes, A. G. & Berger, B. (2010). Sulfosalt melts: evidence of high-temperature vapor transport of metals in the formation of high-sulfidation lode gold deposits. *Economic Geology* **105**, 257–262.

McDonough, W. F. & Sun, S. S. (1995). The composition of the Earth. *Chemical Geology* **120**, 223–253.

McKenzie, D. & O'Nions, R. K. (1991). Partial melt distributions from inversion of rare-earth element concentrations. *Journal of Petrology* **32**, 1021–1091.

McInnes, B. I. A., McBride, J. S., Evans, N. J., Lambert, D. D. & Andrew, A. S. (1999). Osmium isotope constraints on ore metal recycling in subduction zones. *Science* **286**, 512–516.

Meisel, T. & Moser, J. (2004). Platinum-group element and rhenium concentrations in low abundance reference materials. *Geostandards and Geoanalytical Research* **28**, 233–250.

Downloaded from http://petrology.oxfordjournals.org/ by guest on January 20, 2015

Meisel, T., Fellner, N. & Moser, J. (2003). A simple procedure for the determination of platinum group elements and rhenium (Ru, Rh, Pd, Re, Os Ir and Pt) using ID-ICP-MS with an inexpensive on-line matrix separation in geological and environmental materials. *Journal of Analytical Atomic Spectrometry* **18**, 720–726.

Morgan, G. B. & London, D. (2005). Effect of current density on the electron microprobe analysis of alkali aluminosilicate glasses. *American Mineralogist* **90**, 1131–1138.

Mungall, J. E. (2002). Roasting the mantle: Slab melting and the genesis of major Au and Au-rich Cu deposits. *Geology* **30**, 915–918.

Mungall, J. E. & Brenan, J. M. (2014). Partitioning of platinum-group elements and Au between sulfide liquid and basalt and the origins of mantle–crust fractionation of the chalcophile elements. *Geochimica et Cosmochimica Acta* **125**, 265–289.

Nadeau, O., Williams-Jones, A. E. & Stix, J. (2010). Sulphide magma as a source of metals in arc-related magmatic hydrothermal ore fluids. *Nature Geoscience* **3**, 501–505.

Newman, S. & Lowenstern, J. B. (2002). VOLATILECALC: a silicate melt–H_2O–CO_2 solution model written in Visual Basic for Excel. *Computers and Geosciences* **28**, 597–604.

Nimis, P. & Taylor, W. R. (2000). Single clinopyroxene thermobarometry for garnet peridotites. Part I. Calibration and testing of a Cr-in-Cpx barometer and an enstatite-in-Cpx thermometer. *Contributions to Mineralogy and Petrology* **139**, 541–554.

O'Neill, H. S. C. & Mavrogenes, J. A. (2002). The sulfide capacity and the sulfur content at sulfide saturation of silicate melts at 1400°C and 1 bar. *Journal of Petrology* **43**, 1049–1087.

Park, J.-W, Campbell, I. H. & Eggins, S. M. (2012a). Enrichment of Rh, Ru, Ir and Os in Cr spinels from oxidized magmas: evidence from the Ambae volcano, Vanuatu. *Geochimica et Cosmochimica Acta* **78**, 28–50.

Park, J.-W., Hu, Z. C., Gao, S., Campbell, I. H. & Gong, H. J. (2012b). Platinum group element abundances in the upper continental crust revisited—New constraints from analyses of Chinese loess. *Geochimica et Cosmochimica Acta* **93**, 63–76.

Park, J.-W., Campbell, I. H. & Arculus, R. J. (2013a). Platinum-alloy and sulfur saturation in an arc-related basalt to rhyolite suite: Evidence from the Pual Ridge lavas, the Eastern Manus Basin. *Geochimica et Cosmochimica Acta* **101**, 76–95.

Park, J.-W., Campbell, I. H., Ickert, R. B. & Allen, C. M. (2013b). Chalcophile element geochemistry of the Boggy Plain zoned pluton, southeastern Australia: a S-saturated barren compositionally diverse magmatic system. *Contributions to Mineralogy and Petrology* **165**, 217–236.

Paton, C., Hellstrom, J., Paul, B., Woodhead, J. & Hergt, J. (2011). Iolite: Freeware for the visualisation and processing of mass spectrometric data. *Journal of Analytical Atomic Spectrometry* **26**, 2508–2518.

Pearce, J. & Stern, R. J. (2006). Origin of back-arc magmas: Trace element and isotope perspective. In: Christie, D. M., Fisher, C. R., Lee, S.-M. & Givens, S. (eds) *Back-Arc Spreading Systems: Geological, Biological, Chemical, and Physical Interactions. American Geophysical Union, Geophysical Monographs* **166**, 63–86.

Peucker-Ehrenbrink, B., Bach, W., Hart, S. R., Blusztajn, J. S. & Abbruzzese, T. (2003). Rhenium–osmium isotope systematics and platinum group element concentrations in oceanic crust from DSDP/ODP Sites 504 and 417/418. *Geochemistry, Geophysics, Geosystems* **4**, doi: 10.1029/2002GC000414.

Pushkarev, E. V., Kamenetsky, V., Gottman, I. & Yaxley, G. (2014). The PGM-bearing volcanic ankaramaite (Urals, Russia): Bridging ankaramite parental magmas and the Ural–Alaskan-type intrusions. In: Anikina, E. V. et al. (eds) *Proceedings of the 12th International Platinum Symposium, Yekaterinburg, Russia: Institute of Geology and Geochemistry UB RAS*, pp. 204–205.

Putirka, K. D. (2008). Thermometers and barometers for volcanic systems. In: Putirka, K. D. & Tepley, F. J. (eds) *Minerals, Inclusions and Volcanic Processes. Mineralogical Society of America and Geochemical Society, Reviews in Mineralogy and Geochemistry* **69**, 61–111.

Putirka, K. D., Mikaelian, H., Ryerson, F. & Shaw, H. (2003). New clinopyroxene–liquid thermobarometers for mafic, evolved, and volatile-bearing lava compositions, with applications to lavas from Tibet and the Snake River Plain, Idaho. *American Mineralogist* **88**, 1542–1554.

Resing, J. A., Rubin, K. H., Embley, R. W., et al. (2011). Active submarine eruption of boninite in the northeastern Lau Basin. *Nature Geoscience* **4**, 799–806.

Richards, J. P. (2003). Tectono-magmatic precursors for porphyry Cu-(Mo-Au) deposit formation. *Economic Geology and the Bulletin of the Society of Economic Geologists* **98**, 1515–1533.

Richards, J. P. (2011). Magmatic to hydrothermal metal fluxes in convergent and collided margins. *Ore Geology Reviews* **40**, 1–26.

Richards, J. P. & Mumin, A. H. (2013). Lithospheric fertilization and mineralization by Arc Magmas: Genetic links and secular differences between porphyry copper ± molybdenum ± gold and magmatic-Hydrothermal iron oxide copper-gold deposits. In: Colpron, M., Bissig, T., Rusk, B. G. & Thompson, J. F. H. (eds) *Tectonics, Metallogeny, and Discovery: The North American Cordillera and Similar Accretionary Settings.* Society of Economic Geologists, Inc., pp. 277–300.

Righter, K., Chesley, J. T., Geist, D. & Ruiz, J. (1998). Behavior of Re during magma fractionation: an example from Volcan Alcedo, Galapagos. *Journal of Petrology* **39**, 785–795.

Ripley, E. M., Brophy, J. G. & Li, C. S. (2002). Copper solubility in a basaltic melt and sulfide liquid/silicate melt partition coefficients of Cu and Fe. *Geochimica et Cosmochimica Acta* **66**, 2791–2800.

Robb, L. J. (2005). *Introduction to Ore-forming Processes*. Oxford: Blackwell Publishing.

Sato, K. (2012). Sedimentary crust and metallogeny of granitoid affinity: implications from the geotectonic histories of the circum-Japan Sea region, central Andes and southeastern Australia. *Resource Geology* **62**, 329–351.

Seedorff, E., Dilles, J. H., Proffett, J. M., Jr, Einaudi, M. T., Zurcher, L., Stavast, W. J. A., Barton, M. D. & Johnson, D. A. (2005). Porphyry deposits: Characteristics and origin of hypogene features. In: Hedenquist, J. W., Thompson, J. F. H., Goldfarb, R. J. & Richards, J. P. (eds) *Economic Geology. One-hundredth Anniversary Volume 1905–2005*. Littleton, CO: Society of Economic Geologists, pp. 251–298.

Sillitoe, R. H. (2010). Porphyry copper systems. *Economic Geology* **105**, 3–41.

Smith, R. E. (1967). Segregation vesicles in basaltic lava. *American Journal of Science* **265**, 696–713.

Sossi, P. A. & O'Neill, H. C. (2011). Systematic underestimation of the oxidation state of MORB glasses. V. M. Goldschmidt Conference. Mineralogical Magazine **75**, 1915.

Spandler, C. J., Eggins, S. M., Arculus, R. J. & Mavrogenes, J. A. (2000). Using melt inclusions to determine parent-magma compositions of layered intrusions: Application to the Greenhills Complex (New Zealand), a platinum group minerals-bearing, island-arc intrusion. *Geology* **28**, 991–994.

Spandler, C. J., Arculus, R. J., Eggins, S. M., Mavrogenes, J. A., Price, R. C. & Reay, A. J. (2003). Petrogenesis of the

Downloaded from http://petrology.oxfordjournals.org/ by guest on January 20, 2015

Greenhills Complex, Southland, New Zealand: Magmatic differentiation and cumulate formation at the roots of a Permian island-arc volcano. *Contributions to Mineralogy and Petrology* **144**, 703–721.

Sun, S. S. & McDonough, W. F. (1989). Chemical and isotopic systematics of oceanic basalts: implications for mantle composition and processes. In: Saunders, A. D. & Norry, M. J. (eds) *Magmatism in the Ocean Basins.* Geological Society, London, Special Publications **42**, 313–345.

Sun, W. D., Binns, R. A., Fan, A. C., Kamenetsky, V. S., Wysoczanski, R., Wei, G. J., Hu, Y. H. & Arculus, R. J. (2007). Chlorine in submarine volcanic glasses from the eastern Manus basin. *Geochimica et Cosmochimica Acta* **71**, 1542–1552.

Sun, W. D., Zhang, H., Ling, M. X., Ding, X., Chung, S. L., Zhou, J. B., Yang, X. Y. & Fan, W. M. (2011). The genetic association of adakites and Cu–Au ore deposits. *International Geology Review* **53**, 691–703.

Sylvester, P. J. & Eggins, S. M. (1997). Analysis of Re, Au, Pd, Pt and Rh in NIST glass certified reference materials and natural basalt glasses by laser ablation ICP-MS. *Geostandards Newsletter* **21**, 215–229.

Togashi, S. & Terashima, S. (1997). The behavior of gold in unaltered island arc tholeiitic rocks from Izu-Oshima, Fuji, and Osoreyama volcanic areas, Japan. *Geochimica Et Cosmochimica Acta* **61**, 543–554.

Tomkins, A. G., Rebryna, K. C., Weinberg, R. F. & Schaefer, B. F. (2012). Magmatic sulfide formation by reduction of oxidized arc basalt. *Journal of Petrology* **53**, 1537–1567.

Upton, B. G. J. & Wadsworth, W. J. (1971). Rhyodacite glass in Reunion basalt. *Mineralogical Magazine* **38**, 152–159.

Webster, J. D. & Botcharnikov, R. E. (2011). Distribution of sulfur between melt and fluid in S-O-H-C-Cl-Bearing magmatic systems at shallow crustal pressures and temperatures. In: Behrens, H. & Webster, J. D. (eds) *Sulfur in Magmas and Melts: Its Importance for Natural and Technical Processes*. Mineralogical Society of America, Reviews in Mineralogy.

Webster, J. D., Sintoni, M. F. & De Vivo, B. (2009). The partitioning behavior of Cl, S, and H_2O in aqueous vapor- $\pm$ saline-liquid saturated phonolitic and trachytic melts at 200 MPa. *Chemical Geology* **263**, 19–36.

Wilkinson, J. J. (2013). Triggers for the formation of porphyry ore deposits in magmatic arcs. *Nature Geoscience* **6**, 917–925.

Williams-Jones, A. E. & Heinrich, C. A. (2005). 100th Anniversary special paper: Vapor transport of metals and the formation of magmatic–hydrothermal ore deposits. *Economic Geology* **100**, 1287–1312.

Woodland, S. J., Pearson, D. G. & Thirlwall, M. F. (2002). A platinum group element and Re–Os isotope investigation of siderophile element recycling in subduction zones: Comparison of Grenada, Lesser Antilles arc, and the Izu–Bonin arc. *Journal of Petrology* **43**, 171–198.

Zellmer, K. E. & Taylor, B. (2001). A three-plate kinematic model for Lau Basin opening. *Geochemistry, Geophysics, Geosystems* **2**, doi: 10.1029/2000GC000106.

Zimmer, M. M., Plank, T., Hauri, E. H., Yogodzinski, G. M., Stelling, P., Larsen, J., Singer, B., Jicha, B., Mandeville, C. & Nye, C. J. (2010). The role of water in generating the calc-alkaline trend: new volatile data for Aleutian magmas and a new tholeiitic index. *Journal of Petrology* **51**, 2411–2444.

Downloaded from http://petrology.oxfordjournals.org/ by guest on January 20, 2015